CMV-specific clonal expansion of Th1, GZMK$^+$ CD8$^+$, and TEMRA T cells revealed by human PBMC single cell profiling

Authors: Titas Grabauskas[1,2,‡], Luke Trinity[1‡], Chris P. Verschoor[3,4], Djamel Nehar-Belaid[1], Radu Marches[1], Giray Eryilmaz[1], Avinash S. Mahajan[1,2], Sathya Baarathi[1], Asa Thibodeau[1], Emilie Picard[3], Chia-Ling Kuo[2], Kenneth E. Schmader[5], Cathleen Colon-Emeric[5], Heather E. Whitson[5], Silke Paust[1], Adolfo García-Sastre[6-11], Gur Yaari[12], Jacques Banchereau[1,13]*, George A. Kuchel[2,14]*, and Duygu Ucar[1,15]*

Affiliations:
[1]The Jackson Laboratory for Genomic Medicine; Farmington, CT 06030, USA.
[2]University of Connecticut School of Medicine; Farmington, CT 06030, USA.
[3]Health Sciences North Research Institute; NOSM University; Sudbury, ON P3E 2H3, Canada.
[4]Department of Medicine, McMaster University; Hamilton, ON L8S 4L8 Canada
[5]Department of Medicine and Duke Center for the Study of Aging and Human Development (Aging Center), and GRECC, Durham VA Health Care System; Durham, NC 27705, USA.
[6]Department of Microbiology, Icahn School of Medicine at Mount Sinai; New York, NY 10029, USA.
[7]Global Health and Emerging Pathogens Institute, Icahn School of Medicine at Mount Sinai; New York, NY 10029, USA.
[8]Department of Medicine, Division of Infectious Diseases, Icahn School of Medicine at Mount Sinai; New York, NY 10029, USA.
[9]The Tisch Cancer Institute, Icahn School of Medicine at Mount Sinai; New York, NY 10029, USA.
[10]Department of Pathology, Molecular and Cell-Based Medicine, Icahn School of Medicine at Mount Sinai; New York, NY 10029, USA.
[11]The Icahn Genomics Institute, Icahn School of Medicine at Mount Sinai; New York, NY 10029, USA.
[12]Department of Pathology, Yale School of Medicine, New Haven, CT 06510-3222, USA.
[13]Immunoledge LLC; Montclair, NJ 07042, USA.
[14]UConn Center on Aging, University of Connecticut School of Medicine; Farmington, CT 06032, USA.
[15]Institute for Systems Genomics, University of Connecticut Health Center; Farmington, CT 06032, USA.
‡ These authors contributed equally to this work.
* Corresponding authors: duygu.ucar@jax.org, jacques.banchereau@gmail.com, kuchel@uchc.edu

Abstract:

Cytomegalovirus (CMV) is a common herpesvirus that establishes lifelong latency and becomes increasingly prevalent with age. We systematically characterized CMV-associated immune remodeling by analyzing six human cohorts (two newly built) using single-cell RNA sequencing, T cell receptor (TCR) sequencing, and flow cytometry. Beyond the well-known expansion of CD4$^+$/CD8$^+$ TEMRA, adaptive NK, and γδ T cells, CMV(+) adults exhibited increased frequencies of GZMK$^+$ CD8$^+$ T cells and atypical B cells, alongside a reduction of CD56^{dim} NK cells. Longitudinal profiling of an individual who seroconverted revealed rapid CMV-driven shifts in circulating immune cell frequencies. Single-cell TCR data analyzed using a large database of

CMV-associated clones combined with predictive modelling (CMVerify), identified novel CMV-specific clonal expansions reproduced across two independent cohorts. In the $CD8^+$ lineage, CMV-specific clones were enriched in $GZMK^+$ $CD8^+$ and $CD8^+$ TEMRA cells, while in the $CD4^+$ lineage, Th1 cells showed clonal expansion alongside $CD4^+$ TEMRA cells. This integrative study revealed how latent CMV alters the cellular and clonal landscape, defining $GZMK^+$ $CD8^+$ and Th1 cells as newly recognized elements of response to CMV in humans.

Introduction

The immune system undergoes significant changes with aging, characterized by a decline in naïve cell populations, expansion of memory and terminally differentiated T and B cells, and increased pro-inflammatory activity[1,2]. These changes contribute to weakened immune responses and increased susceptibility to disease[1,3,4]. However, the trajectory of immune aging varies widely between individuals[5], leading to differences in immune health, vaccine efficacy, and therapeutic responses[6–8]. Twin studies have shown that immune variability increases with age and non-heritable environmental factors account for a substantial proportion of this inter-individual variation[9]. Notably, cytomegalovirus (CMV) infection has emerged as a key environmental factor, as monozygotic twins discordant for CMV exhibited significant divergence in immune cell traits[9,10].

CMV is a DNA herpesvirus transmitted through bodily fluids[11], that establishes lifelong latency in hematopoietic stem and myeloid progenitor cells[12]. It is one of the most prevalent chronic infections worldwide, with seropositivity increasing with age[13]. According to the CDC, over 50% of adults in the U.S. are infected with CMV by age of 40[14]. Although typically asymptomatic in healthy individuals, latent CMV has been associated with more severe outcomes of SARS-CoV-2[15] and tuberculosis infections[16]. Conversely, CMV seropositivity has also been linked to improved survival following anti-PD-1 checkpoint blockade in older melanoma patients[17], and enhanced influenza vaccine responses in healthy young adults[18]. Despite its widespread prevalence and known impact on immune heterogeneity, CMV serostatus is often unreported in single-cell studies of immune aging[2,19,20], limiting our ability to distinguish age-related changes from those associated with CMV.

A hallmark of CMV seropositivity is the expansion of effector memory and terminally differentiated (TEMRA) $CD4^+$ and $CD8^+$ T cells, observed in both young and older adults[21–25]. This phenomenon, known as "memory inflation," reflects the long-term accumulation of CMV-specific clones, particularly within the TEMRA subset ($CD45RA^+CCR7^-$)[26,27], which can comprise up to 10–30% of the total memory T cell pool[26,28]. Clonal expansion of CMV-specific $CD8^+$ T cels reduces the overall T cell receptor (TCR) repertoire diversity[29–31]. While TEMRA cells remain functional—typically expressing *GZMB*, *PRF1*, and *KLRG1*[2,32] and exhibiting potent cytotoxic capacity[22,26,28]—they have limited proliferative potential[33].

Beyond conventional αβ T cells, Vδ1 γδ T lymphocytes also expand in CMV-positive individuals and display adaptive-like features, including clonal expansion and cytotoxic responses to infected cells[34]. Latent CMV infection has been associated with expansion of adaptive NK cells expressing NKG2C[35,36], an activating receptor that recognizes CMV-derived peptides and restricts viral spread[37,38]. These $NKG2C^+$ NK cells persist long-term and display features of immunological memory[38,39].

While these critical insights were derived largely within specific lineages using protein-level data, the recent availability of high-resolution single-cell multi-omic datasets (e.g., RNA-seq, TCR-seq) across independent cohorts and age groups has now enabled a systematic, unbiased dissection of CMV-associated immune remodeling at unprecedented depth. For this purpose, we took advantage of publicly available single-cell datasets and built two new cohorts of our own (see Methods), uncovering novel cellular and clonal associations with CMV, including clonal expansions in $GZMK^+$ $CD8^+$ and Th1 cells.

103 **Study design: newly built older adult cohort for CMV transcriptional signature discovery**

104 We recruited two cohorts of healthy older adults during 2017-2018 from communities surrounding
105 Hartford, Connecticut, USA, and Sudbury, Ontario, Canada. Cohort 1 comprised 36 healthy older
106 adults (n=17 CMV-positive hereinafter referred to as CMV(+), n=19 CMV-negative referred to as
107 CMV(-)), whose peripheral blood mononuclear cells (PBMCs) were profiled using single-cell
108 RNA sequencing (scRNAseq) and flow cytometry (Fig. 1a). Cohort 2 included 63 older adults
109 (n=40 CMV(+), n=23 CMV(-)) whose PBMCs were profiled using flow cytometry alone[40,41] (Fig.
110 1a). Participants were free from confounding autoimmune diseases, were not undergoing
111 treatments that might influence immune function and composition (e.g., immunotherapy) and were
112 not recently vaccinated before blood collection. CMV serostatus was determined in serum using
113 ELISA for CMV IgG antibodies.

114

115 The median age of Cohort 1 was 71 years old, including men (n=17) and women (n=19). CMV(+)
116 and CMV(-) groups were comparable in age (p=0.90), body mass index (BMI; median 27.8,
117 p=0.51), and frailty index[42] (median 0.085, p=0.50) (Fig. 1b, Extended Data Fig. 1a, and
118 Supplementary Table 1). Other characteristics, including race, cancer history, and medication use,
119 were also evenly distributed between the two groups (Supplementary Table 1).

120

121 Cohort 2 had a median age of 75 years, including men (n=24) and women (n=39). Similar to Cohort
122 1 , the CMV(+) and CMV(-) groups were comparable in age (p=0.11), BMI (median 27.1, p=0.93),
123 and frailty index[42] (median 0.09, p=0.88) (Fig. 1b and Supplementary Table 1). Race and cancer
124 history were also evenly distributed between the groups (Supplementary Table 1).

125

126 **Frequencies of memory $CD8^+$ T and γδ T cells are higher in CMV(+) older adults**

127 PBMCs from Cohort 1 were profiled using scRNAseq, capturing 144,324 cells (n=68,642
128 CMV(+), n=75,682 CMV(-)) after quality control (Fig. 1c,d, and Extended Data Fig. 1b). As a
129 group, CMV(+) individuals had higher frequency of $CD8^+$ T cells compared to CMV(-) individuals
130 (25% vs 11% of PBMCs; p=0.0012; Fig. 1e,f and Extended Data Fig. 1c), confirmed by flow
131 cytometry in Cohort 2 (p<0.001; Fig. 1g and Extended Data Fig. 1d). Absolute $CD8^+$ T cell counts
132 were 1.78-fold higher in CMV(+) individuals (p=0.04; Fig. 1h), and the $CD4^+/CD8^+$ T cell ratio
133 was lower in CMV(+) older adults in both cohorts (Discovery: p=0.006; Validation: p<0.001) (Fig.
134 1i and Extended Data Fig. 1d).
135
136 Clustering of $CD8^+$ T cells (n=24,983) (Fig. 2a and Extended Data Fig. 2a) identified seven
137 subsets: (i) naïve (*CCR7*$^+$, *SELL*$^+$, *LEF1*+), (ii) central memory (CM; *CCR7*$^+$), (iii) mucosal-
138 associated invariant T (MAIT; *ZBTB16*$^+$, *KLRB1*$^+$), (iv) $GZMK^+$ $CD8^+$ (*CCR7*$^-$, *GZMK*$^+$), (v)
139 TEMRA (*GZMB*$^+$, *KLRD1*$^+$), (vi) *GZMK*$^+$ γδ (*TRDC*$^+$, *GZMK*$^+$), and (vii) *GZMB*$^+$ γδ (*TRDC*$^+$,
140 *GZMB*$^+$) cells. All subsets, except MAIT cells, were significantly altered with CMV positivity.
141 $GZMK^+$ $CD8^+$ (p<0.001), TEMRA (p<0.001), and $GZMB^+$ γδ (p<0.001) were subsets with the
142 highest increase in frequency in CMV(+) older adults (Fig. 2b,c and Extended Data Fig. 2b).
143
144 CD8+ TEMRA cells exhibited a 9.5-fold relative expansion in CMV(+) compared CMV(-) adults
145 (7.2% vs 0.8% of PBMCs; p<0.001; Fig. 2c), which was confirmed by flow cytometry in Cohort
146 2 (p<0.001; Fig. 2d and Extended Data Fig. 2c). Absolute $CD8^+$ TEMRA counts supported these
147 results (p=0.001; Fig. 2e). γδ T cells, which recognize antigens independently of MHC
148 presentation[43], were also more frequent in CMV(+) adults, particularly the $GZMB^+$ γδ subset
149 which showed a 5.8-fold increase (3.7% vs 0.6%; p<0.001; Fig. 2c and Extended Data Fig. 2b).
150 Increase in γδ T cell frequency was confirmed in Cohort 2 by flow cytometry (p=0.05; Fig. 2f and

151 Extended Data Fig. 2c). GZMK$^+$ CD8$^+$ T cells were also more frequent in CMV(+) adults (6% vs
152 1.6% of PBMCs; p<0.001; Fig 2c and Extended Data Fig. 2b).
153
154 To assess whether these CMV-associated alterations were specific to older adults, we re-analyzed
155 publicly available scRNA-seq datasets from younger adults (Cohort 3; n=47, 25-35 years old;
156 n=45, 55-65 years old; Extended Data Fig. 2d) with known CMV serostatus (CMV(+) n=42;
157 CMV(-) n=50)[32]. CD8$^+$ TEMRA T, GZMB$^+$ γδ T, and GZMK$^+$ CD8$^+$ T cell frequency was also
158 higher in CMV(+) younger adults (p<0.001; Fig. 2g and Extended Data Fig. 2e).
159
160 In-depth analyses of each CD8$^+$ subset revealed very few differentially expressed genes (DEGs;
161 FDR<0.05) between CMV(+) and CMV(-) older individuals (Supplementary Table 2). To further
162 explore cell-intrinsic differences, we calculated single-cell scores for cytotoxicity and lymphoid
163 innateness—a gradient that evaluates transcriptional similarity of T cells to innate lymphocytes
164 (Supplementary Table 3)[44,45]. These scores were largely comparable between CMV(+) and CMV(-
165) donors across all subsets, except for GZMK$^+$ CD8$^+$ T cells that displayed an increased
166 cytotoxicity score for CMV(+) individuals (Extended Data Fig. 2f, g). Together, CMV
167 seropositivity is associated with substantial compositional remodeling of the CD8$^+$ T cell
168 compartment with minor cell-intrinsic alterations in older adults.
169
170 **Frequency of CD4$^+$ TEMRA T cells is higher in CMV(+) older adults**
171 CD4$^+$ T cells (55,927) (Fig. 2h and Extended Data Fig. 3a) were clustered into four subsets: (i)
172 naïve (*CCR7*$^+$); (ii) T-regulatory cells (Tregs; *FOXP3*$^+$, *TIGIT*$^+$), (iii) effector memory (EM;
173 *S100A4*$^+$, *GZMB*$^-$), and (iv) TEMRA cells (*GZMB*$^+$, *GNLY*$^+$). CMV(+) individuals exhibited a
174 lower frequency of naïve CD4$^+$ T cells (p=0.04) and higher frequency of CD4$^+$ TEMRA cells

175 (p=<0.001; Fig. 2j and Extended Data Fig. 3b). CD4$^+$ TEMRA cells were 6.4-fold higher in
176 CMV(+) individuals (2.15% vs 0.34% of PBMCs), confirmed by flow cytometry in Cohort 2
177 (p=0.009; Figure 2k and Extended Data Fig. 2c). Absolute counts of CD4$^+$ TEMRA cells were
178 also higher in CMV(+) (p=0.08; Fig. 2l). Cohort 3 displayed similar relative expansion of CD4$^+$
179 TEMRA cells (p<0.001; Fig. 2m and Extended Data Fig. 3c). DEG analysis yielded few (n=3)
180 significant genes (Supplementary Table 2), with *CCL5* upregulated in Tregs from CMV(+) older
181 adults.
182
183 Further clustering of the CD4$^+$ memory compartment (EM; n=19,691; Extended Data Fig. 3d)
184 revealed five memory subsets (i) T helper 1 (Th1; *IFNG-AS1*$^+$, *GZMK*$^+$), (ii) T helper 17 (Th17;
185 *RORC*$^+$, *CCR6*$^+$, *CTSH*$^+$), (iii) T follicular helper-like (Tfh-like; *CXCR5*$^+$) (iv) T helper 2 (Th2;
186 *GATA3*$^+$), and (v) T helper 10 (Th10; *CCR10*$^+$)[46]. None of these memory subsets remodeled with
187 CMV seropositivity in our cohort (Extended Data Fig. 3e,f) or in Cohort 3 (Extended Data Fig
188 3g,h).
189
190 Thus, CMV seropositivity in older adults is associated with higher frequency of CD4$^+$ TEMRA
191 cells without alterations of other memory CD4$^+$ T cell subsets.
192
193 **Frequency of atypical B cells (ABCs) is higher in CMV(+) older adults**
194 B cells (n=12,573; Fig. 3a and Extended Data Fig. 4a) clustered into five subsets: (i) naïve (*IL4R*$^+$,
195 *IGHM*$^+$), (ii) transitional (*CD9*$^+$, *MME*$^+$), (iii) ABC (*CD27*$^-$, *ITGAX*/CD11c$^+$, *TBX21*/Tbet$^+$), (iv)
196 memory (*CD27*$^+$, *IGHG1*$^+$, *IGHA1*$^+$), and (v) plasmablasts (PB; *JCHAIN*$^+$, *MZB1*$^+$). CMV(+)
197 individuals had higher frequencies of ABCs, with a 3.4-fold increase (0.27% vs 0.9%; p=0.01; Fig.
198 3b,c and Extended Data Fig.4b). This increase in frequency was also observed in 55–65-year-old

199 CMV(+) individuals from Cohort 3 (p=0.04; Fig. 3d and Extended Data Fig. 4c). No DEGs were
200 found between CMV(+) and CMV(-) older adults in any B cell subset (Supplementary Table 2).
201
202 Therefore, CMV seropositivity is linked with more frequent ABCs without affecting other B cell
203 subsets.
204
205 **Frequency of CD56^{dim}NK cells is lower, whereas frequency of NKG2C^{+} NK cells is higher in**
206 **CMV(+) older adults.**
207 NK cells (n=17,222) (Fig. 3e,f) clustered into three subsets: (i) CD56^{dim} NK cells (*SPON2*$^{+}$,
208 *FCGR3A*$^{+}$, *GZMB*$^{+}$), (ii) CD56^{bright} NK cells (*NCAM1*/CD56 $^{+}$, *GZMK*$^{+}$, *XCL1*$^{+}$), and (iii)
209 KLRC2^{+} NK cells (*KLRC2*$^{+}$/NKG2C), which closely resembled adaptive NK cells (Extended Data
210 Fig. 4d)[47,48].
211
212 CD56^{dim} NK cell frequency was lower in CMV(+) individuals in both our older adult cohort (6.6%
213 vs 12.2% of PBMCs; p=0.02; Fig. 3g,h) and Cohort 3 (p<0.001; Fig. 3j and Extended Data Fig.
214 4e). Conversely, KLRC2^{+} NK cell frequency was higher by 2.3-fold in CMV(+) older adults, (2%
215 vs. 0.8%; p=0.011, Fig. 3h), which was confirmed by flow cytometry in Cohort 2 (p<0.001; Fig.
216 3i and Extended Data Fig. 4f). KLRC2^{+} NK cells were also more frequent in CMV(+) individuals
217 within Cohort 3 (p<0.001; Fig. 3j and Extended Data Fig. 4e). No DEGs were found between
218 CMV(+) and CMV(-) older adults in NK subsets (Supplementary Table 2).
219
220 **Monocyte and dendritic cell frequencies are comparable between CMV(+) and CMV(-) older**
221 **adults**

222 Monocytes (n=30,132) (Fig. 4a and Extended Data Fig. 5a) clustered into four subsets: (i) CD14$^+$
223 monocytes (*CD14*$^+$, *LYZ*$^+$, *S100A8*$^+$, *S100A9*$^+$), (ii) ISG-high CD14$^+$ monocytes (*CD14*$^+$, *IFI44L*$^+$,
224 *MX1*$^+$), (iii) intermediate monocytes (*FCGR3A*$^+$, *CD14*$^+$, *HLA-DRB1*$^+$), and (iv) CD16$^+$ monocytes
225 (*FCGR3A*$^+$, *FCER1G*$^+$). No differences in monocyte subset frequencies or DEGs were observed
226 between CMV(+) and CMV(-) individuals (Fig. 4b, Extended Data Fig. 5b, and Supplementary
227 Table 2). Monocyte subset was also not altered with CMV in Cohort 3 (Extended Data Fig. 5c).
228
229 Dendritic cells (DCs) (Fig. 4c) clustered into five subsets (i) monocyte-derived dendritic cells
230 (Mono-DC; *S100A8*$^+$, *CD14*$^+$, *CLEC10A*$^+$), (ii) type-2 classical dendritic cells (cDC2; *CLEC10A*$^+$,
231 *CD1C*$^+$), (iii) type-1 classical dendritic cells (cDC1; *CLEC9A*$^+$), (iv) AXL$^+$ dendritic cells (AXL$^+$
232 DC; *AXL*$^+$), and (v) plasmacytoid DCs (pDCs; *IRF7*$^+$, *JCHAIN*$^+$). Among these subsets, pDCs
233 showed a trend toward lower frequency in CMV(+) individuals (0.35% vs 0.6% of PBMCs)
234 (p=0.07; Fig. 4, d,e and Extended Data Fig. 5d). A modest but significant reduction in pDC
235 frequency was also observed in Cohort 3 (0.35% vs 0.41%; p=0.03; Fig. 4f and Extended Data
236 Fig. 5e). No DEGs were found between CMV(+) and CMV(-) older adults in DC subsets
237 (Supplementary Table 2).
238
239 Overall, our older adult cohorts revealed pronounced CMV-associated remodeling of lymphoid
240 immune cell subsets, with minimal alterations in myeloid cells (Fig. 4g and Supplementary Table
241 4). To estimate the contribution of clinical factors to lymphocyte frequency variance in Cohort 1 ,
242 we conducted Principal Variance Component Analysis[49] (for exact procedure see supplementary
243 materials under "Data and code availability"), which identified CMV serostatus as the dominant
244 contributor (43%), followed by BMI (11%) (Extended Data Fig. 5g). Finally, leveraging
245 longitudinal samples from Cohort 3, revealed that CMV-associated immune signature remains

246 stable over three years (Fig. 4h and Extended Data Fig. 5f), underscoring the persistent nature of
247 latent CMV-driven immune remodeling.
248
249 **CMVerify: a novel tool that accurately infers CMV serostatus from PBMC scRNA-seq data**
250 To enable analysis of public single-cell RNA-seq studies lacking CMV serostatus information, we
251 developed a machine learning model: CMVerify. This tool leverages a Random Forest
252 classification model that uses PBMC subtype frequencies as input (i.e., data features) to predict
253 latent CMV serostatus (i.e., classification output) (Fig. 5a). CMVerify was trained on Cohort 3
254 (n=92 total; n=42 CMV(+); n=50 CMV(-); Extended Data Fig. 2c) using leave-one-out cross-
255 validation, achieving 96.7% training accuracy. Top predictive features included $CD4^+$ TEMRA,
256 $CD8^+$ TEMRA, $KLRC2^+$ NK cells, and $GZMB^+$ γδ T cells (Extended Data Fig. 6a,b), consistent
257 with our CMV-associated immune signature. We first validated CMVerify in our Discovery
258 Cohort, where it correctly predicted CMV serostatus in 26 out of 27 individuals (Fig. 5b and
259 Extended Data Fig. 6c). We then further tested CMVerify on two independent older adult cohorts
260 with different chemistries using available CMV IgG and PBMC scRNA-seq data: Cohort 4 (n=19,
261 age 62-90) profiled using 10X 3' scRNAseq, Cohort 5: (n=20, age 64-88) profiled using 10X 5'
262 scRNAseq. Across these datasets, CMVerify achieved 97% average accuracy, 98% positive
263 predictive value (PPV), and 96% negative predictive value (NPV) (Fig. 5b, Extended Data Fig.
264 6c).
265
266 To evaluate longitudinal performance, CMVerify was applied to 77 individuals from Cohort 3,
267 each with PBMC scRNA-seq data across 9 timepoints. The model maintained 97% accuracy,
268 correctly classifying 670 of 693 longitudinal samples (Fig. 5c and Extended Data Fig 6d).
269 Misclassifications primarily stemmed from two donors with unusually low $CD4^+$ TEMRA

270 frequencies (Extended Data Fig 6e). Remarkably, in a donor who seroconverted over the study
271 (35-year-old male, ID: BR1049), CMVerify successfully tracked the transition, shifting its
272 prediction from CMV(-) to CMV(+) in parallel with rising CMV IgG titers (Fig. 5c,d). This
273 transition was accompanied by rapid (within months) and dramatic changes in PBMC composition,
274 including a 90.99-fold increase in $CD4^+$ TEMRAs, 8.74-fold increase in $CD8^+$ TEMRAs, and 3.37-
275 fold increase in $KLRC2^+$ NK cells (Fig. 5e and Extended Data Fig. 6f). These analyses established
276 that CMVerify is an effective tool that can be used to infer CMV serostatus from single cell
277 datasets in the absence of serological data.
278
279 **CMV-specific TCR clones are expanded in $GZMK^+$ $CD8^+$ T and Th1 cells**
280 To study how CMV-seropositivity alters T cell clonal diversity, we profiled PBMCs of 20 older
281 adults (Cohort 5) using 10X 5' scRNA-seq with paired TCR sequencing (Fig. 5b and Fig. 6a). We
282 recovered 128,924 high-quality TCRα–TCRβ pairs, averaging 6,446 T cells per donor (Fig. 6a),
283 with comparable cell counts between CMV(-) and CMV(+) groups (Extended Data Fig. 7a). These
284 128,924 T cells represented 103,575 clones, where a clone was defined as a unique TCRα–TCRβ
285 pair at the nucleotide level. We first quantified overall TCR repertoire diversity using the exponent
286 of Shannon's entropy (e^H) across all memory $CD4^+$ and $CD8^+$ T cells for each donor (using the
287 Alakazam package[50], see Methods). CMV(+) donors had reduced overall TCR diversity compared
288 to CMV(-) donors (Fig. 6b and Supplementary Table 5), in line with previous observations[30].
289 Subset-specific analysis revealed that $GZMK^+$ $CD8^+$ T cells exhibited reduced TCR clonal
290 diversity in CMV(+) individuals, in addition to $CD4^+$/$CD8^+$ TEMRA cells (Fig. 6c). Surprisingly,
291 Th1 cells also had lower TCR diversity in CMV(+) individuals (Fig. 6c and Extended Data Fig.
292 7b,c; see Methods), despite showing no change in frequency (Extended Data Fig. 3f).
293

294 To identify putative CMV-specific TCRs, we leveraged the CMV ECOcluster, a recently curated
295 database of 26,106 TCRβ sequences enriched in over 12,000 CMV(+) individuals[51]. A subset of
296 the ECOcluster TCRβ chains were previously experimentally validated as responding CMV
297 peptides via the VDJdb database[52] (primarily pp65 and IE1; see Methods; Supplementary Table
298 5). By matching exact V–J pairings and CDR3 amino acid sequences between the CMV
299 ECOcluster and TCR-seq data from our cohort, we identified 493 putative CMV-specific cells
300 (Fig. 6d) from 115 clones (see Methods). In CMV(-) donors, we identified a small population (32
301 cells from 30 clones; Extended Data Fig. 7d) of naïve $CD4^+$ T cells (based on their scRNA-seq
302 transcriptional profile; Extended Data Fig. 7e,f), consistent with stochastic V(D)J recombination
303 in naïve T cells[53,54] and absence of antigen-driven differentiation (Fig. 6d). In contrast, CMV(+)
304 donors had clonally expanded CMV-specific T cells (461 cells from 85 clones; Fig. 6d and
305 Extended Data Fig. 7a,e). As expected, the highest frequencies of putative CMV-specific cells
306 were detected within the $CD4^+$ TEMRA (mean clonal expansion: 11.5x) and $CD8^+$ TEMRA
307 (10.6x) subsets (Fig. 6d and Extended Data Fig. 7g). CMV-specific TCRs were also expanded
308 within the $GZMK^+$ $CD8^+$ T cells (4.4x; Fig. 6d and Extended Data Fig. 7g), consistent with their
309 increased frequency (Fig. 2c) and reduced TCR diversity (Fig. 6c). Finally, the Th1 helper subset
310 contained a modest expansion of CMV-specific clones (1.5x) (Fig. 6d and Extended Data Fig. 7g),
311 in line with its decreased TCR diversity (Fig. 6c).
312
313 To validate our observations in an independent cohort, we obtained a publicly available PBMC
314 scRNA-seq dataset with paired scTCR-seq from 166 donors (aged 25–81 years, Cohort 6)[2] (Fig.
315 6e). Since CMV serostatus was not reported, we first used CMVerify to obtain CMV serostatus
316 predictions. To increase confidence in our downstream analysis, we independently confirmed and
317 refined CMVerify predictions with the CMV ECOcluster (see Methods) to confidently resolve

318 CMV serostatus of 135 donors: 85 predicted CMV(-) and 50 predicted CMV(+) (Fig. 6e, Extended
319 Data 7h, and Supplementary Table 6). We identified 626,427 high-quality TCRα–β pairs
320 (averaging 4,640 per donor) and repeated our TCR diversity analysis in this cohort. Reproducing
321 our findings in Cohort 5, CMV(+) individuals in Cohort 6 also had reduced overall TCR diversity
322 and CMV-specific clonal expansion, particularly within $CD4^+/CD8^+$ TEMRA, $GZMK^+$ $CD8^+$ T,
323 and Th1 subsets (Fig. 6f,g, Extended Data 7i, and Supplemental Table 6). In total, we identified
324 141 CMV-specific cells in CMV(-) individuals (mostly within the naïve $CD4^+$ T subset) and 3,410
325 CMV-specific cells in CMV(+) individuals (Fig. 6g). Importantly, in CMV(+) individuals, these
326 CMV-specific cells were detected in $CD4^+/CD8^+$ TEMRA, $GZMK^+$ $CD8^+$ T, and Th1 subsets, as
327 observed in our Cohort 5 (Fig. 6g). Overall, across both cohorts, the average CMV(-) individual
328 possessed one $CD4^+$ naïve CMV-specific cell (Fig. 6h). In contrast, CMV(+) individuals had an
329 average of 73 CMV-specific cells, of which 71% were $CD4^+/CD8^+$ TEMRA, 15% were $GZMK^+$
330 $CD8^+$ T and 8% were Th1 cells (Fig. 6h).
331
332 By analyzing single-cell RNA-seq paired with TCR-seq data across two cohorts, we showed that
333 within the $CD8^+$ lineage, there is CMV clonal expansion of $GZMK^+$ $CD8^+$ T cells in addition to
334 $CD8^+$ TEMRA cells[55]. Within the $CD4^+$ lineage, CMV-specific clones were detected in Th1 cells
335 along with $CD4^+$ TEMRA cells[33].
336
337 **Discussion**
338 This is the most comprehensive study of CMV-associated changes in cellular composition and
339 clonal diversity, integrating data from six human cohorts spanning different age groups, including
340 two newly built older adult cohorts. We confirmed known associations in $CD4^+/CD8^+$ TEMRA T
341 cells[24,26,32,33,55,56], γδ T cells[34], and $KLRC2^+$ (adaptive) NK cells[35,36]. Importantly, we expand these

342 immune signatures by showing that: (i) GZMK^{+} CD8^{+} T cells are increased in frequency and
343 display CMV-specific clonal expansion, (ii) CD4^{+} Th1 helper cells exhibit CMV-specific clonal
344 expansion, and (iii) atypical B cells are increased in frequency and CD56^{dim} NK cells are reduced
345 in CMV(+) individuals across age groups.
346
347 GZMK^{+} CD8^{+} T cells have been traditionally linked to aging and inflammaging[2,2,57]. Here, we
348 show that these cells are increased in frequency with latent CMV, exhibit reduced TCR diversity,
349 and harbor expanded CMV-specific clones in both younger and older CMV(+) adults, supporting
350 a direct role for CMV in their expansion. Similar GZMK signatures were also observed in human
351 tissues with latent CMV[58]. GZMK is a tryptase-like protease recently shown to activate
352 complement cascade, initiating a lymphocyte-driven inflammatory response[59]. These data suggest
353 that inflammation may also contribute to the immune control of viral latency, in addition to the
354 well-defined cytotoxic responses (e.g., CD4^{+}/CD8^{+} TEMRA and adaptive NK cells). How
355 inflammatory and cytotoxic pathways and cell types interact to sustain CMV control, however,
356 remains to be elucidated.
357
358 Our TCR analyses across two independent cohorts uncovered Th1 cells as the only CD4^{+} T helper
359 subset harboring CMV-specific clones expanded in CMV(+) individuals, albeit with smaller clone
360 sizes. These findings suggest that CMV-driven clonal expansion occurs within the CD4^{+} T helper
361 subset but appears more tightly regulated as compared to CD4^{+} TEMRA cells. Future studies will
362 be essential to understand how Th1 cells contribute to latent CMV responses, e.g., by helping
363 cytotoxic lymphocyte proliferation[60] and/or stimulating CMV-specific antibody formation via
364 ABCs (Fig. 3c,d).
365

366 CMV serostatus is often missing in scRNA-seq datasets, despite its known influence on immune
367 phenotypes. To retrospectively analyze such datasets, we developed CMVerify—a machine
368 learning classifier that predicts CMV serostatus from single-cell transcriptomic data with high
369 accuracy. We provide CMVerify as an open-source tool for the research community. Prior tools
370 can leverage cytometry[61] or TCR-seq[62] data to predict CMV serostatus, while CMVerify is the
371 first model to do so using scRNA-seq data. Despite being trained on a younger adult cohort,
372 CMVerify accurately predicted CMV status across three independent older adult cohorts,
373 highlighting the robust and age-independent imprint of CMV on immune cell compositions.
374 Furthermore, CMVerify successfully captured a seroconversion event, highlighting rapid (within
375 months) PBMC compositional shifts linked to acute/latent CMV. CMVerify was instrumental in
376 reproducing our CMV-specific TCR analyses and novel observations in GZMK^{+} CD8^{+} T and Th1
377 cells by allowing us to infer CMV status in a public dataset[2].
378
379 Our comprehensive multi-modal study revealed novel CMV-associated changes in cellular
380 composition and TCR diversity, including the clonal expansion of GZMK^{+} CD8^{+} T and Th1 cells
381 in CMV(+) individuals. Future studies should aim to understand how cytotoxic (CD4^{+}/CD8^{+}
382 TEMRA T cells), inflammatory (GZMK^{+} CD8^{+} T cells), and T helper (Th1 cells) cells orchestrate
383 effective control of latent CMV in healthy adults.
384
385 **Limitations**
386 Our study has several limitations. First, the exciting results observed in CMV seroconversion are
387 unfortunately based on a single case (n = 1). Out of ~250 individuals followed over two years,
388 only one seroconversion event was captured. Therefore, substantially larger cohorts will be needed
389 to capture additional seroconversion events and establish a causal relationship between CMV

390 infection and the rapid remodeling of circulating immune cell populations. Second, the CMV
391 ECOcluster was derived from enrichment analyses and has not yet been fully experimentally
392 validated. While the ECOcluster is large and highly specific (with some TCRs mapping to the
393 experimentally validated VDJdb database; see Methods), further experimental validation of these
394 TCR sequences will be instrumental. Despite these limitations, our study provides valuable and
395 novel insights into the systemic effects of latent CMV infection across multiple cohorts and age
396 groups.
397

398 **Materials and Methods**

399

400 **Cohort Descriptions**

401

402 **Cohort 1** (n=36) comprised individuals recruited from two separate studies:

403 1. UConn Center on Aging Bacterial Pneumonia Vaccine Study: Twenty healthy older adults
404 aged 60 years and older were recruited at the University of Connecticut Center on Aging
405 during the 2017 and 2018 seasons (IRB number: 16-071J; R01AG052608; R01AI142086).
406 Participants did not have confounding treatments or conditions that would influence
407 immune function and composition (e.g., immunotherapy, immunosuppressive disorders,
408 and prednisone in doses greater than 10 mg/day)[63].

409 2. Immune Response to High-Dose vs. Standard Dose Influenza Vaccine at the University of
410 Connecticut Health Center (UCHC): Sixteen healthy older adults aged 65 years and older
411 were recruited at UCHC and Health Sciences North Research Institute (HSNRI) in 2017 to
412 study resilience to influenza infections. Exclusion criteria for these participants included

413 known immunosuppressive disorders or medications, including prednisone in doses greater
414 than 10 mg/day.

415 The CMV(+) and CMV(-) groups in Cohort 1 had comparable distributions in age, sex, body mass
416 index (BMI), frailty index, medication use, and cancer history (see Supplementary Table 1).

417

418 **Cohort 2** (n=63): This publicly available dataset[40,41] was profiled via flow cytometry. It consisted
419 of healthy older adults (66-92 years old). The CMV(+) and CMV(-) groups in Cohort 2 had
420 comparable distributions in age, sex, BMI, frailty index, and cancer history (see Supplementary
421 Table 1).

422

423 **Cohort 3** (n=96): This publicly available dataset[32] was profiled using 10X 3' scRNA-seq and
424 included longitudinal samples from n=49 healthy young adults (25-35 years old) and n=47 healthy
425 older adults (55-65 years old).

426

427 **Cohort 4** (n=19): This publicly available dataset[64] was profiled using 10X 3' scRNA-seq and
428 included n=95 samples, of which we used n=19 samples (62-90 years old) with known CMV
429 serology (ELISA) data.

430

431 **Cohort 5** (n=20): Healthy older adults (64-88 years old) were recruited at the University of
432 Connecticut Center on Aging during the 2022-2023 seasons (IRB number: 2022-Ceded-002) and
433 profiled using 10X 5' scRNA-seq with paired scTCR-seq. Participants did not have confounding
434 treatments or conditions that would influence immune function and composition (e.g.,
435 immunotherapy, immunosuppressive disorders, and prednisone in doses greater than 10 mg/day).

436 The CMV(+) and CMV(-) groups in Cohort 5 had comparable distributions in age, sex, BMI,
437 ongoing cancer diagnosis, and frailty index (see Supplementary Table 1).

438

439 **Cohort 6** (n=166): This publicly available dataset[2] was profiled using 10X 5' scRNA-seq with
440 paired scTCR-seq and included longitudinal samples from n=166 healthy adults (25-81 years old).

441

442 **Summary of Cohorts Used in the Study**
443

Cohort name	Originating Study	Modality	Age range	CMV seropositivity	Purpose of use
Cohort 1	Grabauskas et al.	a) 10X 3' scRNA-seq b) Flow cytometry	60-88	CMV(-): 22 CMV(+): 21	a) Derive CMV-linked immune signatures b) Test CMVerify
Cohort 2	Verschoor et al. Picard et al.	Flow cytometry	66-92	CMV(-): 23 CMV(+): 40	Validate CMV-linked immune signatures
Cohort 3	Gong et al.	10X 3' scRNA-seq	26-66	CMV(-): 52 CMV(+): 44	a) Validate CMV-linked immune signatures b) Train CMVerify
Cohort 4	Nehar-Belaid et al.	10X 3' scRNA-seq	62-90	CMV(-): 7 CMV(+): 12	Test CMVerify
Cohort 5	Grabauskas et al.	a) 10X 5' scRNA-seq b) scTCR-seq	64-88	CMV(-): 14 CMV(+): 6	a) Test CMVerify b) CMV-linked TCR analysis
Cohort 6	Terekhova et al.	a) 10X 5' scRNA-seq b) scTCR-seq	25-80	NA	Validate CMV-linked TCR findings

444 **Table 1.** Summary of cohorts used in this study. For each cohort, the table lists the source, profiling
445 modality of PBMCs, age distribution, CMV seropositivity distribution, and the specific purpose
446 of use in this study.

447

448 **Sample Collection in Cohort 1 and Cohort 5**

449 In Cohort 1 and Cohort 5, peripheral blood mononuclear cells (PBMCs) were isolated by
450 Lymphoprep (StemCell Technologies) gradient centrifugation within 1h after collection of blood
451 samples by Lymphoprep (StemCell Technologies) gradient centrifugation whereas serum was
452 isolated from the blood collected in red top collection tubes (BD Vacutainer). The isolated PBMCs
453 were resuspended in a cryoprotective solution containing 90% FBS and 10% DMSO, then
454 transferred to liquid nitrogen for long-term storage whereas serum was stored at -80°C.

455

456 **Cytomegalovirus Serostatus in Cohort 1 and Cohort 5**

457 CMV serostatus was determined by ELISA using the CMV IgG ELISA kits (Aviva Systems
458 Biology and Genesis Diagnostics Ltd; see Supplementary Table 1). Serum samples were thawed
459 at room temperature, diluted, and analyzed according to manufacturer's recommendations.
460 Calculation of the results was done based on the appropriate controls included in the kit.

461

462 **10X 3' Single-Cell Library Preparation and Sequencing in Cohort 1**

463 In Cohort 1, we generated a total of 27 baseline PBMC scRNA-seq samples from older adults as
464 part of two separate studies. All of these samples were generated at the Jackson Laboratory Single
465 Cell Biology Lab using the same pipeline. Briefly, cells were washed and resuspended in PBS
466 containing 0.04% BSA and immediately processed as follows. Cell viability was assessed on a
467 Countess FL II automated cell counter (Thermofisher) using Trypan Blue staining, and up to
468 12,000 cells from each suspension were loaded onto one lane of a 10x Genomics Chip G. Single
469 cell capture, barcoding, and library preparation were performed using the 10x Genomics
470 Chromium Controller platform version 3.1 NEXTGEM chemistry and according to the
471 manufacturer's protocol (CG000315, 10x Genomics). cDNA and libraries were assessed for

472 quality via Tapestation 4200 (Agilent) and Qubit fluorometer (ThermoFisher), quantified by
473 KAPA qPCR, and sequenced on a NovaSeq 6000 (Illumina) S4 v1.5 200 flow cell using a 28-10-
474 10-90 asymmetric read configuration targeting a read depth of 50,000 per cell.
475
476 **10X 5' Single-Cell Library Preparation and Sequencing in Cohort 5**
477 In Cohort 5, we generated a total of 20 baseline PBMC scRNA-seq samples from older adults. All
478 samples were generated at the Jackson Laboratory Single Cell Biology Lab using the same
479 pipeline. After dissociation, cells were washed and suspended in PBS containing 0.04% BSA and
480 immediately processed as follows. Cell viability was assessed on a LUNA FX7 automated cell
481 counter (Logos Biosystems) via AO/PI staining, and up to 29,000 cells from each suspension were
482 loaded onto one lane of a 10x Genomics Chromium GEM-X Single Cell 5' Chip v3. Single cell
483 capture, barcoding and library preparation were performed using the 10x Genomics Chromium X
484 platform[65] 5' version 3 GEM-X chemistry and according to the manufacturer's protocol
485 (CG000733, revA). From each individual sample, cDNA was derived and used for the construction
486 of a gene expression and a TCR (VDJ) library. cDNA and libraries were checked for quality by
487 Tapestation 4200 (Agilent) and Qubit Fluorometer (ThermoFisher) and quantified by KAPA
488 qPCR. Libraries were sequenced on an Illumina NovaSeq X+ 25B 300 cycle flow cell, with a 28-
489 10-10-90 (R1-I1-I2-R2) asymmetric read configuration, targeting 20,000 barcoded cells with an
490 average sequencing depth of 50,000 reads per cell and 15,000 reads per cell for the gene expression
491 and TCR library.
492
493 **scRNA-seq preprocessing in Cohort 1, Cohort 3, and Cohort 5**
494 In Cohort 1 and Cohort 5, Illumina base call files for all libraries were converted to FASTQs using
495 bcl2fastq v2.20.0.422 (Illumina, CA, USA) and FASTQ files associated with baseline gene

496 expression libraries were aligned to the GRCh38 reference assembly with v32 annotations from
497 GENCODE (10x Genomics GRCh38 reference 2020-A) using the version 6.1.1 Cell Ranger count
498 pipeline (10x Genomics, CA, USA), as previously described[63]. The resulting gene-cell expression
499 matrices, were then corrected for ambient RNA contamination using SoupX[66]. The corrected gene-
500 cell expression matrices were then used for downstream analysis. We used the Scrublet[67] package
501 in Python to estimate the doublet score for each sample with an estimated doublet set to 0.1.
502 Doublets were manually confirmed to be doublets via expression of PBMC lineage markers before
503 being removed from downstream analyses. Cells with (i) genes that were not detected in at least 3
504 cells, (ii) mitochondrial reads greater than 25% (20% in Cohort 5), and (iii) fewer than 200 features
505 were excluded. Filtered gene expression matrices were merged and processed using the Scanpy
506 toolkit (version 1.9.1)[68]. Read counts were log normalized to the total number of reads in each
507 individual cell to count-per-million (CPM) using the "normalized_total" and "log1p" functions.
508 Genes with the highest normalized dispersion were identified using the "highly_variable_genes"
509 function. Gene expression matrices were scaled using "scale" function and Principal Component
510 Analysis (PCA) was performed using the "pca" function. To correct batch effects across samples
511 at the PBMC level, we applied Harmony[69] in Cohort 1 and Cohort 5. To correct batch effects
512 across samples at the lineage level, we applied Harmony in Cohort 1 and SCVI-Tools[70] in Cohort
513 5. For the baseline samples, 100 Principal Components (PCs) were used to calculate nearest
514 neighbors via the "neighbors" function which were used to perform uniform manifold
515 approximation and projection (UMAP) *via* the "umap" function. Initial clusters were determined
516 using the "leiden" function (resolution=0.8) for all PBMCs. Multiple rounds of marker
517 identification, cell type annotation, and manual inspection and doublet removal, were performed
518 to annotate PBMC subsets in Cohort 1 and Cohort 5.
519

520 In Cohort 3, our compositional analysis focused on the Flu Year 1 Day 0 baseline time point (Fig.
521 2g,m, Extended Data Fig. 2c, Fig.3d,j, and Fig.4f), which included n=1,539,411 cells. This dataset
522 was filtered—by the original authors—for doublets using Scrublet and further refined by removing
523 cells with more than 5,000 genes or fewer than 200 genes, and mitochondrial threshold over 10%.
524 The only additional threshold we imposed for automated quality control was to remove genes
525 detected in less than 3 cells, which left 32,069 genes detected. Cells were clustered and annotated
526 using the same process we applied to Cohort 1. In Figure 2h we also include annotations following
527 the above procedure for Flu Year 2 Day 0 (Yr 2 V1) and Year 3 Stand-Alone (Yr 3 V1) timepoints.
528 Finally, in Figure 5e for the seroconverter we annotated cells from all available timepoints.
529

530 ***CMVerify* model training**

531 Baseline samples (Flu Year 1 Day 0) from Cohort 3 (n=92)[32] were used for training *CMVerify*. The
532 input to our machine learning pipeline was donor-level PBMC frequencies of the 72 cell types,
533 labeled with the Allen Institute for Immunology Level 3 (High Resolution, i.e., AIFI_L3)
534 CellTypist model[32,71]. PBMC frequencies were scaled using "StandardScaler" as provided by the
535 scikit-learn package[72] to transform frequencies to have zero mean and unit variance. A random
536 forest classifier was used for model training. Optimal parameters were selected using grid search
537 and leave-one-out cross-validation over all possible combinations of the following
538 hyperparameters:

Parameter	*Grid Search Options* ***(selected)***
number of estimators	50, **100**, 200
max depth	**None**, 10, 20, 30
minimum samples to split internal node	2, **5**, 10
minimum samples required at a leaf	1, 2, **4**
number of features to consider when looking for best split	**square root (number of features)**, $\log_2$ (number of features)

sampling with replacement	True, **False**

Table 2: Parameters tested and selected (in bold) for *CMVerify* training.

Optimal parameters (indicated in bold in Table 2) yielded the best cross validation score of 0.967.

Feature importances were calculated based on the mean decrease in impurity where impurity is a measure of how mixed a node in a tree is with respect to target labels. Features (cell type frequencies) that best reduce the impurity and more effectively split the CMV(+) and CMV(-) samples will have the highest importance (Extended Data Fig. 6a, Table 3). Fourteen features were selected by *CMVerify* based on feature importance scores (Table 3). To evaluate how the Cell Typist labeling corresponds with our Discovery Cohort cell type labels (see Methods:scRNA-seq data analyses), we mapped the top five *CMVerify* selected Cell Typist features to our own cell type annotations (Extended Data Fig. 6b).

Cell Type	*Importance*
KLRF1- GZMB+ CD27- memory CD4 T cell ($CD4^+$ TEMRA)	0.351594
KLRF1- GZMB+ CD27- EM CD8 T cell ($CD8^+$ TEMRA)	0.162693
Adaptive NK cell ($KLRC2^+$ NK)	0.137851
KLRF1- effector Vd1 gdT ($GZMB^+$ γδ)	0.092140
KLRF1+ effector Vd1 gdT ($GZMB^+$ γδ)	0.090094
Proliferating NK cell	0.033280
GZMK- CD27+ EM CD8 T cell	0.026493
GZMK+ CD56dim NK cell	0.025931
GZMK- CD56dim NK cell	0.024149
KLRF1+ GZMB+ CD27- EM CD8 T cell	0.018953
ISG+ CD56dim NK cell	0.010061
GZMK+ memory CD4 Treg	0.009613
pDC	0.009209
CD8 MAIT	0.007939

Table 3: Fourteen features were selected by *CMVerify* during training procedure, listed here in descending order of importance (for predicting CMV serostatus).

555 **TCR analyses in Cohort 5**

556 Samples from Cohort 5 were processed using the same methods as described above (see Methods:
557 scRNA-seq preprocessing in Cohort 1, Cohort 3, and Cohort 5). Cells were annotated based on
558 their scRNA-seq transcriptional profiles, and paired TCR-seq data was analyzed following the
559 Scirpy pipeline[73]. Before quality control, we obtained 159,626 cells which had paired TCR-seq
560 data, of which 14% had more than one pair of TCRs, and 5% had orphan TCRs. We excluded
561 those 29,605 cells that did not have a single pair from the analysis. We also excluded cells
562 annotated as γδ T cells, leaving 128,924 $CD4^+/CD8^+$ T cells with a single pair TCR after quality
563 control (6,446 cells on average from each donor, see Fig. 6a). Cell counts were comparable
564 between CMV(-) and CMV(+) donors (see Extended Data Fig. 7a); although CMV(+) donors had
565 more $CD4^+$ TEMRA (Supplementary Table 5). We computed the distance between TCR using the
566 identity metric at the nucleotide level, defining the clonotypes based on both receptor arms'
567 primary chain[73] (Table 4).

TCR Parameters (Scirpy, i.e., ir, and Alakazam)	*Value*
ir.pp.ir_dist metric	identity
ir.tl.define_clonotypes receptor_arms	all
ir.tl.define_clonotypes dual_ir	primary_only
estimateAbundance nboot	200
estimateAbundance uniform	TRUE
estimateAbundance min_n (memory repertoire)	1000
estimateAbundance min_n (celltype repertoire)	30

568 **Table 4**: Parameters for TCR analysis via Scirpy and Alakazam to enable reproducibility. Column
569 one lists the function name and then specific parameters with parameter value in column two.

570

571 To estimate TCR diversity per cell type, we computed the Hill Diversity Index ^qD[74] where
572 q=1, (i.e., the exponent of Shannon Entropy, e^H), using the 'estimateAbundance' method from the
573 Alakazam package[50]. We used the uniform sampling parameter to control for differences in cell
574 counts between donors, i.e., all samples were 'downsampled' to the minimum across samples

575 during the procedure which included 200 bootstrap replicates (Table 4). To measure CMV-specific
576 clonal expansion in the memory compartment (see Fig. 6b), we excluded naïve $CD4^+$, naïve $CD8^+$,
577 and naïve Treg cells. To identify subset specific differences in repertoire diversity between CMV(-
578) and CMV(+) donors, we again used the 'estimateAbundance' function (same parameters as
579 above), with the additional restriction that each donor must have at least 30 cells within the subset
580 to be included in the comparison (see Fig. 6c and Extended Data Fig.7c).
581

582 **Putative CMV-specific TCR identification in Cohort 5 and Cohort 6**

583 To identify putative CMV-specific TCRs, we searched the CMV ECOcluster[51] (see
584 Methods: CMV ECOcluster) for exact matches with TCR in Cohort 5 and Cohort 6, i.e., identical
585 TCRβ V gene, J gene and CDR3 amino acid sequence. Using Cohort 5 (with known CMV IgG
586 serology via ELISA), we established a CMV-specific clone fraction cutoff that divided our CMV(-
587) and CMV(+) donors: all CMV(-) donors had <0.1% of their total clones matched as CMV-
588 specific (see Extended Data Fig. 7d). CMV-specific clone fraction for each individual was
589 calculated as follows:

590 $$\frac{CMV specific\ clones}{total\ clones}$$

591

592 **CMV status prediction in Cohort 6**

593 We applied CMVerify to predict CMV status in Cohort 6 using the 1,916,367 PBMCs from 166
594 donors who each had samples across 1-3 timepoints. We applied CMVerify for each sample and
595 timepoint. In total, 94 donors were consistently predicted CMV(-) and 65 were consistently
596 predicted as CMV(+) across all timepoints (see Extended Data Fig. 7h). We excluded seven donors
597 with inconsistent CMVerify predictions as unresolved. To further refine our predictions and
598 increase confidence in the downstream analysis, we utilized our established cutoff (based on

599 Cohort 5 where CMV serostatus was determined with CMV IgG ELISA; see Extended Data Fig.
600 7d and Methods: Putative CMV-specific TCR identification in Cohort 5 and Cohort 6) of <0.1%
601 of total clones matched as CMV-specific. Specifically, we excluded: (i) CMVerify predicted
602 CMV(-) individuals with CMV-specific clone proportion ≥0.1%, and (ii) CMVerify predicted
603 CMV(+) individuals with CMV-specific clone proportion <0.1% (see Fig. 6e). To summarize, we
604 confidently resolved 135/166 donors CMV serostatus in Cohort 6, with 50 individuals predicted
605 CMV(+) and 85 individuals predicted CMV(-) (see Fig. 6e).
606
607 **TCR analyses in Cohort 6**
608 Cohort 6 contained 738,718 single pair TCR from donors across the lifespan[2] (see Fig 6e). We
609 first downloaded their publicly available single-cell RNA- and TCR-seq data, matching the donor
610 metadata using paired barcodes. We followed an identical TCR quality control procedure as
611 described above. Note that we made three minor changes to their scRNA-seq cell annotations to
612 enable better comparison with Cohort 6 annotations: (1) combining $CD8^+$ Tem $GZMB^+$ and $CD8^+$
613 TEMRA to be called $CD8^+$ TEMRA (both were *GZMB*$^+$), (2) combining $CD4^+$ Terminal effector
614 and $CD4^+$ TEMRA to be called $CD4^+$ TEMRA (both were $GZMB^+$), and (3) combining Th1/Th17
615 and Th1 to be called Th1 (both were IFNG-AS1$^+$, $GZMK^+$). Due to low cell counts (compared to
616 Cohort 5), we combined TCR data from all timepoints for each individual in the TCR diversity
617 calculations. Overall cell counts were comparable between predicted CMV(-) and CMV(+)
618 (Supplementary Table 6); although predicted CMV(+) donors had more $CD4^+$/$CD8^+$ TEMRA,
619 $GZMK^+$ $CD8^+$, Proliferative $CD8^+$, and $KLRC2^+$ $CD8^+$ (Supplementary Table 6). We computed
620 the Hill Diversity index for each individual's memory repertoire using 98 donors that met the
621 criteria for inclusion (minimum number of cells 1000, see Table 4). We followed the same
622 procedure to compute subset level repertoire diversity as described above (see Fig 6f and Methods:

623 TCR analyses in Cohort 5). To identify CMV-specific TCRs in Cohort 6, we followed the same
624 procedure as described above (see Methods: Putative CMV-specific TCR identification in Cohort
625 5 and Cohort 6).
626 We provide antigen gene information, cell type breakdown, donor metadata, and all alpha and beta
627 chain information at both amino acid and nucleotide level for all CMV-specific clones identified
628 in Cohort 5 and Cohort 6 (see Supplementary Table 5, 6).
629
630 **CMV ECOcluster**
631 To identify CMV-specific TCRs, we obtained the publicly available CMV ECOcluster (Exposure
632 Co-Occurrence cluster)[51] which was previously identified using a multi-stage procedure outlined
633 in brief as follows. First, HLA genotypes were measured from direct sequencing of 4,144 subjects,
634 in combination with bulk TCR (>200,000 T cells sequenced) for each individual, to identify
635 1,000,000 public TCR statistically associated with HLA[75]. Leveraging the co-ocurrence patterns
636 of HLA-restricted TCRs, in combination with bulk TCR data from 30,674 individuals, a single
637 TCR cluster was identified for each of 7 common exposures: EBV, HSV-1, HSV-2, Parvovirus,
638 T. gondii, CMV, and SARS-CoV-2[76]. Finally, the CMV ECOCluster, which comprises 26,106
639 TCRs, was made publicly available[51]. Note that this approach is based solely on the combination
640 of TCRβ V gene, J gene and CDR3 amino acid sequence.
641 To validate CMV ECOcluster specificity, we examined whether any CMV ECOcluster TCRβ
642 chains had been previously identified in the VDJdb database[52], which includes 23,755
643 experimentally-validated CMV-specific TCRβ chains. Among these, 737 CMV-specific TCRβ
644 chains overlapped with the CMV ECOcluster dataset: pp65 (534 matches), IE1 (111 matches), IE2
645 (89 matches), and pp50 (3 matches). To estimate background matching, we also quantified
646 overlaps with non-CMV-specific TCRβ chains in VDJdb, identifying 398 matches out of 86,818

647 non-CMV-specific TCRβ chains. Fisher's exact test revealed a highly significant enrichment of
648 overlap between putative CMV-specific TCRβ chains from the ECOcluster and experimentally
649 validated CMV-specific TCRβ chains in VDJdb (odds ratio=6.65, $p<0.0001$). This result indicates
650 that putative CMV-specific sequences were over six times more likely to occur among validated
651 CMV-specific TCRs than expected by chance, supporting the robustness of CMV ECOcluster and
652 its specificity.
653
654 To identify putative CMV-specific TCRβ chains in Cohort 5, we processed our TCRβ chains from
655 IMGT format[77] to enable exact matching (based on identical TCRβ V gene, J gene and CDR3
656 amino acid sequence) with the CMV ECOcluster.
657
658 **Differential expression analyses in Cohort 1**
659 Raw RNA counts were aggregated across cell types using the function "ADPBulk" from adpbulk
660 package (GitHub: noamteyssier, 2021, adpbulk). For each cell type, samples containing fewer than
661 10 cells were excluded from the differential analysis. Raw counts were first converted to a
662 "DGEList" object, and transformed to normalized matrices using the "calcNormFactors" and
663 "cpm" functions in edgeR[78]. Genes with zero normalized counts across all samples within a given
664 cell type were removed. Differentially expressed gene (DEG) analysis was performed using
665 generalized linear models, employing the default normalization method based on the trimmed
666 mean of M-values (TMM) and controlling for batch, sex and site of sample collection. P-values
667 were adjusted using Benjamini–Hochberg correction for multiple comparisons and genes with an
668 adjusted P-value (FDR) < 0.05 were selected as DEGs.
669
670 **Batch correction for gene expression in Cohort 1**

671 In Cohort 1, our scRNA-seq samples included two scRNA-seq libraries (previously published,
672 n=11; and unpublished, n=16) that were sequenced separately. Batch effects were corrected as
673 follows: For each cell type of interest, raw RNA counts were aggregated at the donor level
674 (pseudobulk) as described above. Next, pseudobulk matrix values were adjusted for batch using
675 pyComBat[79]. Finally, the mean expression of genes of interest were calculated at the donor level
676 using batch-corrected pseudobulk matrix.
677
678 **Gene scoring in Cohort 1**
679 Cytotoxicity score for each sample was calculated by computing the mean expression of
680 "Cytotoxic lymphocytes" (M9.1) gene set in $CD8^+$ T cells [44] (n=29 genes, Supplementary Table
681 3). Innateness score was calculated by computing the mean expression of innateness-related genes
682 in $CD8^+$ T cells[45] (n=80 genes, Supplementary Table 3).
683
684 **Flow cytometry data generation and analyses in Cohort 1**
685 The absolute counts of the major cell populations in PBMCs from CMV(+) and CMV(-)
686 individuals in Cohort 1 were labeled and analyzed as follows. Fluorescent-labeled antibody
687 cocktails for cell-surface staining panels were pre-mixed in BD Horizon Brilliant Stain Buffer (BD
688 Biosciences) 10 minutes before staining. Antibody cocktails were added over 100 µL aliquots of
689 anticoagulated whole blood in a 5 ml FACS tube within 60 minutes of blood collection. Samples
690 were incubated for 15 minutes at room temperature then lysed and fixed with 2 ml of 1x FACS
691 lysing solution (BD Biosciences) for 8 minutes at room temperature. The lysed samples were
692 washed twice to remove the unbound antibodies, lysed RBCs, and platelets and finally resuspended
693 in 250 µL of PBS to which 50 µL of count beads suspension (Count Bright Absolute Counting
694 Beads, Thermo Fisher) were added for the detection of absolute cell counts. Cells were stained

695 with fluorochrome-labeled antibodies to the following surface markers: CD3 (clone UCHT1,
696 BioLegend), CD4 (clone RPA-T4, BD Biosciences), CD8 (clone SFC121Thy2D3, Beckman-
697 Coulter), CD19 (clone HIB19, BD Biosciences), CD14 (clone MSE2, BD Biosciences), CD197
698 (clone 150503, BD Biosciences), and CD45RA (clone HI100, BD Biosciences), and CD127 (clone
699 HIL-7R-M21, BD Biosciences). The stained cells were acquired with LSR Fortessa X-20 (BD)
700 and analyzed with FlowJo software (BD).
701
702 **Statistical tests**
703 In Cohort 1, Cohort 2, and Cohort 5, categorical participant characteristics including sex, race,
704 previous cancer diagnosis, and medications used were compared using Fisher's exact test (two-
705 sided) or the chi-square test, as applicable, using the SciPy package (GitHub: SciPy, 2011).
706
707 Across the study, Mann-Whitney U test (two-sided) was performed to compare CMV(+) and
708 CMV(-) groups for continuous variables (e.g., age, BMI, and frailty), cell frequencies and gene set
709 scores (e.g., Cytotoxicity score, Innateness score). Unless stated otherwise in figure legends, p-
710 values in the main and supplementary figures are reported after multiple hypothesis testing
711 correction (i.e. q) by Benjamini-Hochberg's procedure at FDR < 0.05.
712
713 **Ethics Approval for Cohort 1, Cohort 2, and Cohort 5**
714 The study protocols were approved by the Institutional Review Board of the University of
715 Connecticut Health Center (UConn Health IRB #20-130-J-1 or JAX IRB #2019-006-JGM and
716 IRB# - 2022-Ceded-002) and the Health Sciences North Research Ethics Board (#985). Written
717 informed consent was obtained from all participants prior to inclusion in the study.
718

References and Notes

1. Nikolich-Žugich, J. The twilight of immunity: emerging concepts in aging of the immune system. *Nat Immunol* **19**, 10–19 (2018).
2. Terekhova, M. *et al*. Single-cell atlas of healthy human blood unveils age-related loss of NKG2C+GZMB−CD8+ memory T cells and accumulation of type 2 memory T cells. *Immunity* **56**, 2836-2854.e9 (2023).
3. Guo, J. *et al*. Aging and aging-related diseases: from molecular mechanisms to interventions and treatments. *Sig Transduct Target Ther* **7**, 1–40 (2022).
4. Kennedy, B. K. *et al*. Geroscience: linking aging to chronic disease. *Cell* **159**, 709–713 (2014).
5. Mogilenko, D. A., Shchukina, I. & Artyomov, M. N. Immune ageing at single-cell resolution. *Nat Rev Immunol* **22**, 484–498 (2022).
6. Nehar-Belaid, D. *et al*. Baseline immune states (BIS) associated with vaccine responsiveness and factors that shape the BIS. *Seminars in Immunology* **70**, 101842 (2023).
7. Hou, Y. *et al*. Insights into vaccines for elderly individuals: from the impacts of immunosenescence to delivery strategies. *npj Vaccines* **9**, 1–13 (2024).
8. Bartleson, J. M. *et al*. SARS-CoV-2, COVID-19 and the aging immune system. *Nat Aging* **1**, 769–782 (2021).
9. Brodin, P. *et al*. Variation in the Human Immune System Is Largely Driven by Non-Heritable Influences. *Cell* **160**, 37–47 (2015).
10. Yan, Z. *et al*. Aging and CMV discordance are associated with increased immune diversity between monozygotic twins. *Immunity & Ageing* **18**, 5 (2021).
11. Cannon, M. J., Hyde, T. B. & Schmid, D. S. Review of cytomegalovirus shedding in bodily fluids and relevance to congenital cytomegalovirus infection. *Reviews in Medical Virology* **21**, 240–255 (2011).

12. Schwartz, M. & Stern-Ginossar, N. Rethinking human cytomegalovirus latency reservoir. *Annals of the New York Academy of Sciences* **1524**, 30–36 (2023).
13. Staras, S. A. S. *et al.* Seroprevalence of Cytomegalovirus Infection in the United States, 1988–1994. *Clinical Infectious Diseases* **43**, 1143–1151 (2006).
14. CDC. About Cytomegalovirus. *Cytomegalovirus (CMV) and Congenital CMV Infection* https://www.cdc.gov/cytomegalovirus/about/index.html (2025).
15. Alanio, C. *et al.* Cytomegalovirus Latent Infection is Associated with an Increased Risk of COVID-19-Related Hospitalization. *The Journal of Infectious Diseases* **226**, 463 (2022).
16. Kua, K. P., Chongmelaxme, B. & Lee, S. W. H. Association Between Cytomegalovirus Infection and Tuberculosis Disease: A Systematic Review and Meta-Analysis of Epidemiological Studies. *The Journal of Infectious Diseases* **227**, 471–482 (2023).
17. Milotay, G. *et al.* CMV serostatus is associated with improved survival and delayed toxicity onset following anti-PD-1 checkpoint blockade. *Nat Med* 1–15 (2025) doi:10.1038/s41591-025-03647-1.
18. Furman, D. *et al.* Cytomegalovirus infection improves immune responses to influenza. *Sci Transl Med* **7**, 281ra43 (2015).
19. Hashimoto, K. *et al.* Single-cell transcriptomics reveals expansion of cytotoxic CD4 T cells in supercentenarians. *Proc Natl Acad Sci U S A* **116**, 24242–24251 (2019).
20. Zhu, H. *et al.* Human PBMC scRNA-seq–based aging clocks reveal ribosome to inflammation balance as a single-cell aging hallmark and super longevity. *Science Advances* **9**, eabq7599 (2023).
21. Looney, R. J. *et al.* Role of Cytomegalovirus in the T Cell Changes Seen in Elderly Individuals. *Clinical Immunology* **90**, 213–219 (1999).
22. Vescovini, R. *et al.* Naïve and memory CD8 T cell pool homeostasis in advanced aging: impact of age and of antigen-specific responses to cytomegalovirus. *Age (Dordr)* **36**, 625–640 (2014).

768 23. Czesnikiewicz-Guzik, M. *et al.* T cell subset-specific susceptibility to aging. *Clin Immunol* **127**,
769 107–118 (2008).
770 24. Wertheimer, A. M. *et al.* Aging and Cytomegalovirus Infection Differentially and Jointly Affect
771 Distinct Circulating T Cell Subsets in Humans. *The Journal of Immunology* **192**, 2143–2155
772 (2014).
773 25. van der Heiden, M. *et al.* Differential effects of Cytomegalovirus carriage on the immune
774 phenotype of middle-aged males and females. *Sci Rep* **6**, 26892 (2016).
775 26. Wallace, D. L. *et al.* Human cytomegalovirus-specific CD8+ T-cell expansions contain long-lived
776 cells that retain functional capacity in both young and elderly subjects. *Immunology* **132**, 27–38
777 (2011).
778 27. Kuijpers, T. W. *et al.* Frequencies of Circulating Cytolytic, CD45RA+CD27−, CD8+ T Lymphocytes
779 Depend on Infection with CMV1. *J Immunol* **170**, 4342–4348 (2003).
780 28. Sylwester, A. W. *et al.* Broadly targeted human cytomegalovirus-specific CD4+ and CD8+ T cells
781 dominate the memory compartments of exposed subjects. *The Journal of Experimental Medicine*
782 **202**, 673 (2005).
783 29. Krishna, C., Chowell, D., Gönen, M., Elhanati, Y. & Chan, T. A. Genetic and environmental
784 determinants of human TCR repertoire diversity. *Immunity & Ageing* **17**, 26 (2020).
785 30. Zahid, H. J., May, D., Robins, H. & Greissl, J. A Fundamental Relationship between TCR Diversity,
786 Repertoire Size and Systemic Clonal Expansion: Insights from 30,000 TCRβ Repertoires.
787 2025.05.06.652462 Preprint at https://doi.org/10.1101/2025.05.06.652462 (2025).
788 31. Khan, N. *et al.* Cytomegalovirus seropositivity drives the CD8 T cell repertoire toward greater
789 clonality in healthy elderly individuals. *J Immunol* **169**, 1984–1992 (2002).
790 32. Gong, Q. *et al.* Longitudinal Multi-omic Immune Profiling Reveals Age-Related Immune Cell
791 Dynamics in Healthy Adults. 2024.09.10.612119 Preprint at
792 https://doi.org/10.1101/2024.09.10.612119 (2024).

793 33. Libri, V. *et al*. Cytomegalovirus infection induces the accumulation of short-lived, multifunctional
794 CD4+ CD45RA+ CD27− T cells: the potential involvement of interleukin-7 in this process.
795 *Immunology* **132**, 326–339 (2011).
796 34. Pitard, V. *et al*. Long-term expansion of effector/memory Vδ2− γδ T cells is a specific blood
797 signature of CMV infection. *Blood* **112**, 1317–1324 (2008).
798 35. Béziat, V. *et al*. NK cell responses to cytomegalovirus infection lead to stable imprints in the
799 human KIR repertoire and involve activating KIRs. *Blood* **121**, 2678–2688 (2013).
800 36. Schlums, H. *et al*. Cytomegalovirus Infection Drives Adaptive Epigenetic Diversification of NK
801 Cells with Altered Signaling and Effector Function. *Immunity* **42**, 443–456 (2015).
802 37. Watzl, C. Adaptive responses of innate lymphocytes. *Nat Immunol* **19**, 426–427 (2018).
803 38. Hammer, Q. *et al*. Peptide-specific recognition of human cytomegalovirus strains controls
804 adaptive natural killer cells. *Nat Immunol* **19**, 453–463 (2018).
805 39. Béziat, V. *et al*. NK cell responses to cytomegalovirus infection lead to stable imprints in the
806 human KIR repertoire and involve activating KIRs. *Blood* **121**, 2678–2688 (2013).
807 40. Verschoor, C. P. *et al*. NK- and T-cell granzyme B and K expression correlates with age, CMV
808 infection and influenza vaccine-induced antibody titres in older adults. *Front Aging* **3**, 1098200
809 (2023).
810 41. Picard, E. *et al*. Markers of systemic inflammation are positively associated with influenza
811 vaccine antibody responses with a possible role for ILT2(+)CD57(+) NK-cells. *Immun Ageing* **19**,
812 26 (2022).
813 42. Loeb, N. *et al*. Frailty Is Associated With Increased Hemagglutination-Inhibition Titers in a 4-Year
814 Randomized Trial Comparing Standard- and High-Dose Influenza Vaccination. *Open Forum*
815 *Infectious Diseases* **7**, ofaa148 (2020).
816 43. Deseke, M. & Prinz, I. Ligand recognition by the γδ TCR and discrimination between homeostasis
817 and stress conditions. *Cell Mol Immunol* **17**, 914–924 (2020).

818 44. Rinchai, D. *et al.* BloodGen3Module: blood transcriptional module repertoire analysis and
819 visualization using R. *Bioinformatics* **37**, 2382–2389 (2021).
820 45. Gutierrez-Arcelus, M. *et al.* Lymphocyte innateness defined by transcriptional states reflects a
821 balance between proliferation and effector functions. *Nat Commun* **10**, 687 (2019).
822 46. Caielli, S. *et al.* A CD4+ T cell population expanded in Lupus blood provides B cell help through
823 IL10 and succinate. *Nat Med* **25**, 75–81 (2019).
824 47. Vivier, E., Tomasello, E., Baratin, M., Walzer, T. & Ugolini, S. Functions of natural killer cells. *Nat*
825 *Immunol* **9**, 503–510 (2008).
826 48. Rebuffet, L. *et al.* High-dimensional single-cell analysis of human natural killer cell
827 heterogeneity. *Nat Immunol* **25**, 1474–1488 (2024).
828 49. Abdi, H. & Williams, L. J. Principal component analysis. *WIREs Computational Statistics* **2**, 433–
829 459 (2010).
830 50. Gupta, N. T. *et al.* Change-O: a toolkit for analyzing large-scale B cell immunoglobulin repertoire
831 sequencing data. *Bioinformatics* **31**, 3356–3358 (2015).
832 51. May, D. H., Woodhouse, S., Howie, B. & Robins, H. S. A Catalog of the Public T-cell Response to
833 Cytomegalovirus. 2024.05.08.593237 Preprint at https://doi.org/10.1101/2024.05.08.593237
834 (2024).
835 52. Shugay, M. *et al.* VDJdb: a curated database of T-cell receptor sequences with known antigen
836 specificity. *Nucleic Acids Res* **46**, D419–D427 (2018).
837 53. Gellert, M. V(D)J recombination: RAG proteins, repair factors, and regulation. *Annu Rev Biochem*
838 **71**, 101–132 (2002).
839 54. Schatz, D. G. & Swanson, P. C. V(D)J recombination: mechanisms of initiation. *Annu Rev Genet*
840 **45**, 167–202 (2011).
841 55. Griffiths, S. J. *et al.* Age Associated Increase of Low Avidity CMV-Specific CD8+ T Cells That Re-
842 Express CD45RA. *J Immunol* **190**, 5363–5372 (2013).

843 56. Sylwester, A. W. *et al.* Broadly targeted human cytomegalovirus-specific CD4+ and CD8+ T cells
844 dominate the memory compartments of exposed subjects. *J Exp Med* **202**, 673–685 (2005).
845 57. Angarola, B. L. *et al.* Comprehensive single-cell aging atlas of healthy mammary tissues reveals
846 shared epigenomic and transcriptomic signatures of aging and cancer. *Nat Aging* **5**, 122–143
847 (2025).
848 58. Wells, S. B. *et al.* Multimodal profiling reveals tissue-directed signatures of human immune cells
849 altered with age. *Nat Immunol* **26**, 1612–1625 (2025).
850 59. Donado, C. A. *et al.* Granzyme K activates the entire complement cascade. *Nature* **641**, 211–221
851 (2025).
852 60. Mosmann, T. R. & Sad, S. The expanding universe of T-cell subsets: Th1, Th2 and more.
853 *Immunology Today* **17**, 138–146 (1996).
854 61. Hu, Z., Tang, A., Singh, J., Bhattacharya, S. & Butte, A. J. A robust and interpretable end-to-end
855 deep learning model for cytometry data. *Proceedings of the National Academy of Sciences* **117**,
856 21373–21380 (2020).
857 62. Zhou, K. *et al.* Applying T-classifier, binary classifiers, upon high-throughput TCR sequencing
858 output to identify cytomegalovirus exposure history. *Sci Rep* **13**, 5024 (2023).
859 63. Ravichandran, S. *et al.* Distinct baseline immune characteristics associated with responses to
860 conjugated and unconjugated pneumococcal polysaccharide vaccines in older adults. *Nat*
861 *Immunol* **25**, 316–329 (2024).
862 64. Nehar-Belaid, D. *et al.* Single-cell map of the healthy human immune system across the lifespan
863 reveals unique infant immune signatures. 2025.07.28.667181 Preprint at
864 https://doi.org/10.1101/2025.07.28.667181 (2025).
865 65. Zheng, G. X. Y. *et al.* Massively parallel digital transcriptional profiling of single cells. *Nat*
866 *Commun* **8**, 14049 (2017).

867 66. Young, M. D. & Behjati, S. SoupX removes ambient RNA contamination from droplet-based
868 single-cell RNA sequencing data. *GigaScience* **9**, giaa151 (2020).
869 67. Wolock, S. L., Lopez, R. & Klein, A. M. Scrublet: Computational Identification of Cell Doublets in
870 Single-Cell Transcriptomic Data. *Cell Syst* **8**, 281-291.e9 (2019).
871 68. Wolf, F. A., Angerer, P. & Theis, F. J. SCANPY: large-scale single-cell gene expression data analysis.
872 *Genome Biology* **19**, 15 (2018).
873 69. Korsunsky, I. *et al.* Fast, sensitive and accurate integration of single-cell data with Harmony. *Nat*
874 *Methods* **16**, 1289–1296 (2019).
875 70. Gayoso, A. *et al.* A Python library for probabilistic analysis of single-cell omics data. *Nat*
876 *Biotechnol* **40**, 163–166 (2022).
877 71. Domínguez Conde, C. *et al.* Cross-tissue immune cell analysis reveals tissue-specific features
878 in humans. *Science* **376**, eabl5197 (2022).
879 72. Pedregosa, F. *et al.* Scikit-learn: Machine Learning in Python. *Journal of Machine Learning*
880 *Research* **12**, 2825–2830 (2011).
881 73. Sturm, G. *et al.* Scirpy: a Scanpy extension for analyzing single-cell T-cell receptor-sequencing
882 data. *Bioinformatics* **36**, 4817–4818 (2020).
883 74. Hill, M. O. Diversity and Evenness: A Unifying Notation and Its Consequences. *Ecology* **54**, 427–
884 432 (1973).
885 75. Zahid, H. J. *et al.* Large-scale statistical mapping of T-cell receptor β sequences to Human
886 Leukocyte Antigens. 2024.04.01.587617 Preprint at https://doi.org/10.1101/2024.04.01.587617
887 (2024).
888 76. May, D. H. *et al.* Identifying immune signatures of common exposures through co-occurrence of
889 T-cell receptors in tens of thousands of donors. 2024.03.26.583354 Preprint at
890 https://doi.org/10.1101/2024.03.26.583354 (2024).

77. Lefranc, M.-P. *et al.* IMGT®, the international ImMunoGeneTics information system®. *Nucleic Acids Res* **37**, D1006–D1012 (2009).

78. Robinson, M. D., McCarthy, D. J. & Smyth, G. K. edgeR: a Bioconductor package for differential expression analysis of digital gene expression data. *Bioinformatics* **26**, 139–140 (2010).

79. Behdenna, A. *et al.* pyComBat, a Python tool for batch effects correction in high-throughput molecular data using empirical Bayes methods. *BMC Bioinformatics* **24**, 459 (2023).

Acknowledgments:

We gratefully acknowledge the contribution of the Single Cell Biology service, Genome Technologies service, and Cyberinfrastructure high performance computing resources at The Jackson Laboratory (JAX) for assistance with the work described herein. These shared services are supported in part by the JAX Cancer Center (P30 CA034196). We thank Olivia Bart for help with dbGAP data upload. We thank members of the Ucar lab for critical feedback during the progress of the study.

Funding:

This study was made possible by generous financial support of the National Institutes of Health (NIH) grants under award number:

- UH2 AG056925 (to G.K, CCE, J.B., D.U.)
- U01 AI165452 (to D.U., G.K.)
- P30AG067988 Older Americans Independence Pepper Center (to G.A.K., R.M., D.U.)
- P30AG028716 Duke Older Americans Independence Center (to K.E.S, C.C.E, H.E.W).
- NIH grant U19 AI168631 (to A.G.-S.)
- CRIPT (Center for Research on Influenza Pathogenesis and Transmission), a as NIAID-funded Center of Excellence for Influenza Research and Response (CEIRR, contract # 75N93021C00014) (to A.G.S.)
- 1T32AG062409-01A1 (to L.T.)

Other partial sources of funding include:

- JAX Cancer Center (P30 CA034196)
- American Heart Association Predoctoral Fellowship (24PRE1186316) (to T.G.)

Author contributions:

Conceptualization: JB, GK, DU

Methodology: JB, GK, CPV, DU

Investigation: TG, CPV, LT, AT, DN-B, RM, EP, KES, CCE, HEW, SP, AGS, CK, GY

Visualization: TG, LT, GE

Funding acquisition: JB, GK, CCE, DU

Project administration: TG, DU

Supervision: JB, GK, DU

Writing – original draft: TG, CPV, DU, LT

Writing – review & editing: TG, CPV, DU, JB, GK, LT, AT, DN-B, RM, CK, EP, KES, CCE, HEW, SP, AGS, GY

Competing interests:

The A.G.-S. laboratory has received research support from Avimex, Dynavax, Pharmamar, 7Hills Pharma, ImmunityBio and Accurius, outside of the reported work. A.G.-S. has consulting agreements for the following companies involving cash and/or stock: Castlevax, Amovir, Vivaldi Biosciences, Contrafect, 7Hills Pharma, Avimex, Pagoda, Accurius, Esperovax, Applied Biological Laboratories, Pharmamar, CureLab Oncology, CureLab Veterinary, Synairgen, Paratus, Pfizer, Virofend and Prosetta, outside of the reported work. A.G.-S. has been an invited speaker in meeting events organized by Seqirus, Janssen, Abbott, Astrazeneca and Novavax. A.G.-S. is inventor on patents and patent applications on the use of antivirals and vaccines for the treatment and prevention of virus infections and cancer, owned by the Icahn School of Medicine at Mount Sinai, New York, outside of the reported work. G.Y. serves as an advisor to Clareo Biosciences Inc. and holds equity in the company.

Data and code availability:

- Processed data and figure code is available on Synapse (under accession code https://doi.org/10.7303/syn68150215). Data are also browsable online (https://latent-cmv-older-adults-400136930153.us-central1.run.app). Raw read data will be made available on dbGAP upon acceptance of the manuscript (under accession code phs003598.v1.p1). *CMVerify* is available as a Python package: https://pypi.org/project/CMVerify/; open source code hosted at https://github.com/UcarLab/CMVerify.

960 **FIGURE 1**

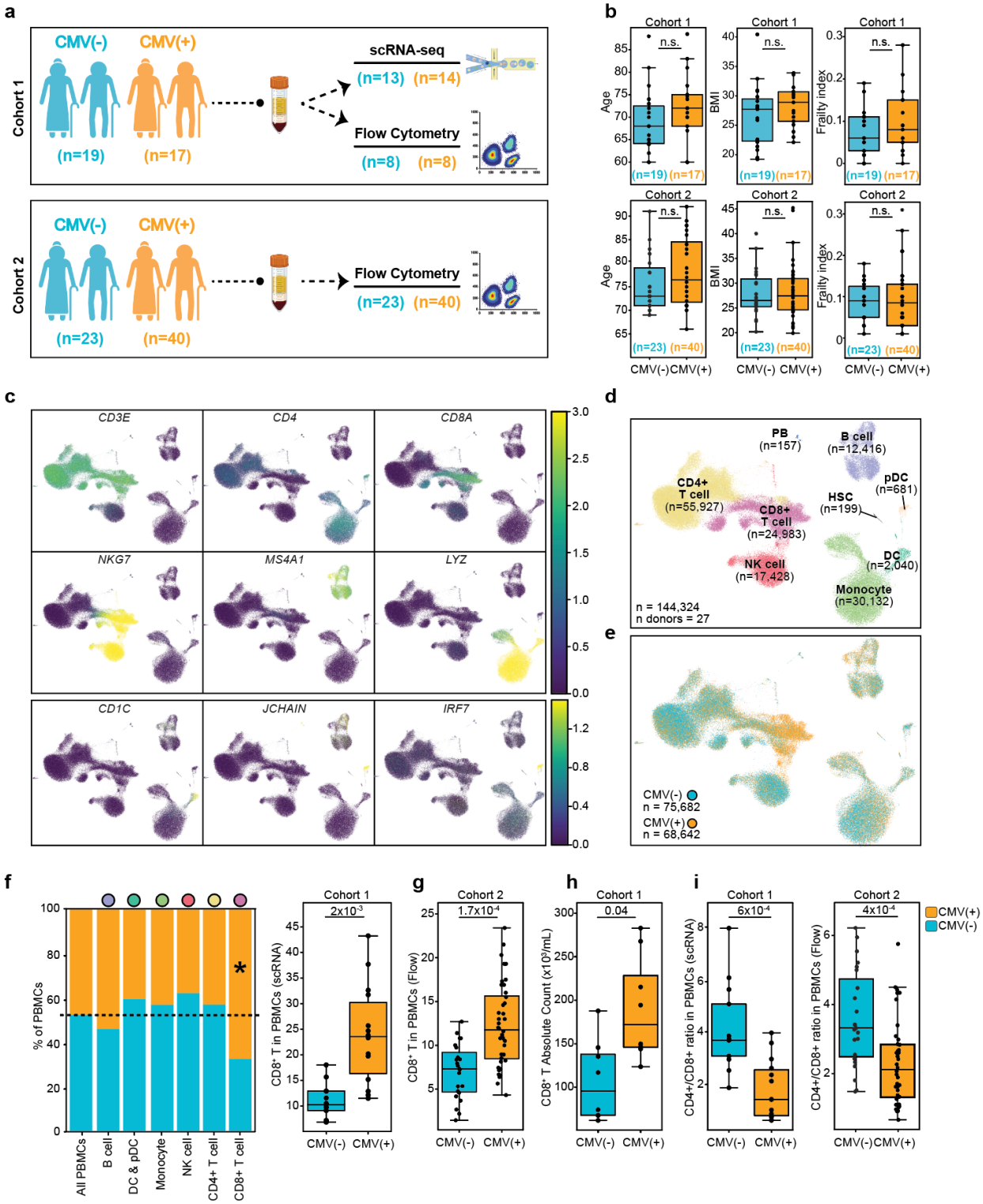

961

962 **Fig. 1| Study design and CD8⁺ T cell subset expansion associated with CMV. a,** Schematic
963 representation of the study design with two cohorts. *Top panel*: Discovery Cohort included n=19
964 CMV(-) and n=17 CMV(+) older adults. *Lower panel*: Validation Cohort included n=23 CMV(-)
965 and n=40 CMV(+) older adults. **b,** Distribution of age, BMI, and frailty index for CMV(-) and
966 CMV(+) groups in Discovery Cohort (*top panel*) and Validation Cohort (*bottom panel*). n.s.

967 indicates not significant. **c,** Uniform manifold approximation and projection (UMAP) representing
968 PBMCs from Discovery Cohort showing expression of subset-specific marker genes. **d,** 9 subsets
969 (n=144,324) colored by immune cell annotations. NK, natural killer; pDC, plasmacytoid dendritic
970 cell; PB, plasmablast; HSC, hematopoietic stem-cell. **e,** UMAP colored for CMV serostatus. **f,**
971 *Left*: Immune cell frequencies in CMV(-) and CMV(+). Cell types with significant frequency
972 differences between CMV(-) and CMV(+) groups are marked with an asterisk (*; P-adjusted
973 [Benjamini-Hochberg] < 0.05). *Right*: Individual-level quantification of $CD8^+$ T cells within
974 PBMCs in CMV(-) (n=13) and CMV(+) (n=14). **g,** $CD8^+$ T cell frequency within PBMCs
975 quantified by flow cytometry in Validation Cohort: CMV(-) (n=23) and CMV(+) (n=40). **h,**
976 Absolute count of $CD8^+$ T cells quantified by flow cytometry in Discovery Cohort: CMV(-) (n=8)
977 and CMV(+) (n=8). **i,** *Left*: $CD4^+$ to $CD8^+$ T cell frequency ratios quantified *via* scRNA-seq in
978 Discovery Cohort: CMV(-) (n=13) and CMV(+) (n=14). *Right:* $CD4^+$ to $CD8^+$ T cell frequency
979 ratios quantified by flow cytometry in Validation Cohort: CMV(-) (n=23) and CMV(+) (n=40).
980 Box plots display the median and IQR (25–75%), with whiskers representing the upper and lower
981 quartiles ±1.5× IQR. Each dot represents an individual sample. Mann-Whitney-U test (two-sided)
982 was used to compare cell counts between CMV(-) and CMV(+) (**b, f, g, h, i**). All *P*-values are
983 shown after adjusting for multiple hypothesis testing using Benjamini-Hochberg at false discovery
984 rate (FDR) < 0.05.
985
986

FIGURE 2

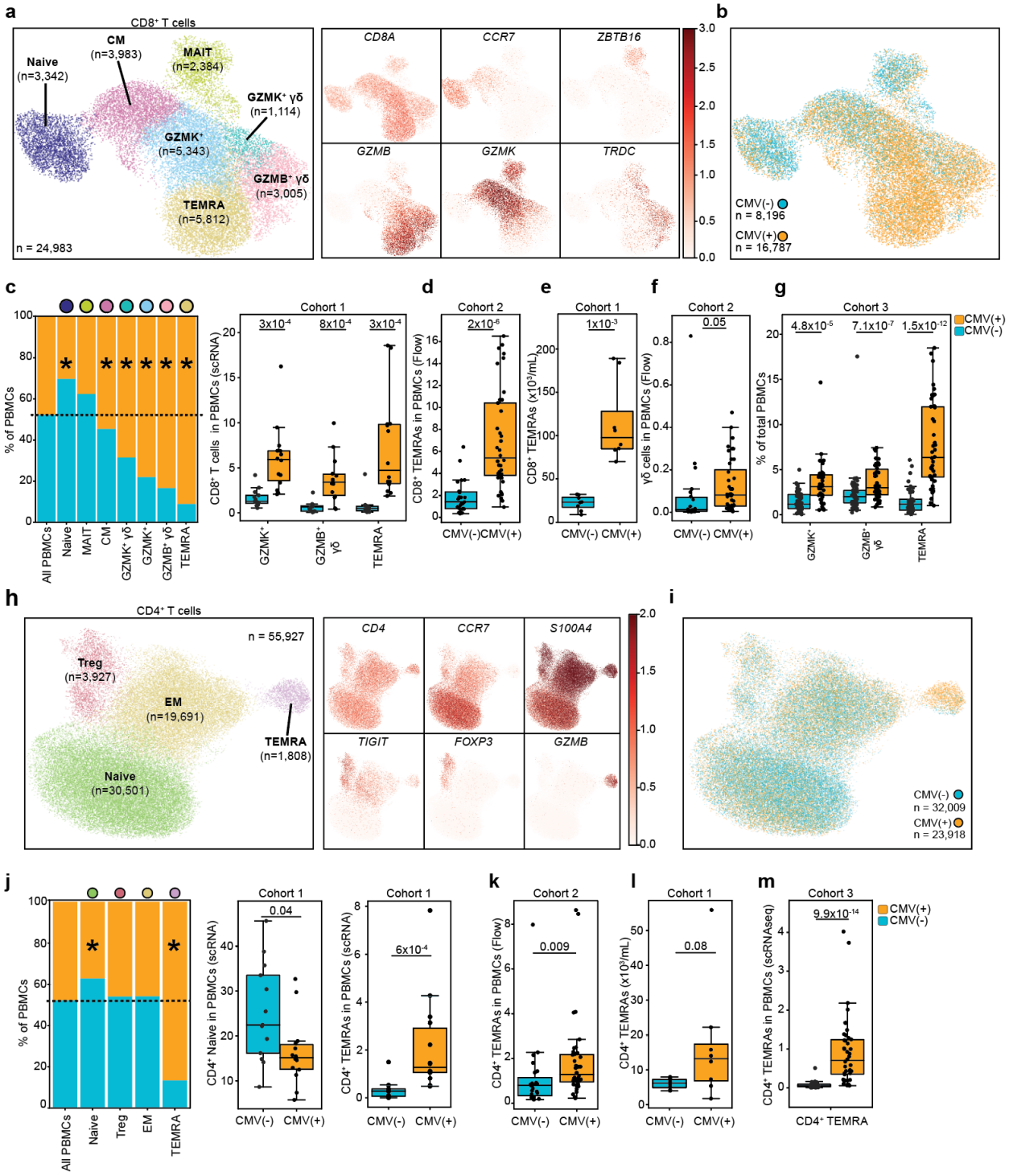

Fig. 2| Expansion of memory CD8⁺ T, γδ T, and CD4⁺ TEMRA cell subsets associated with CMV positivity. a, *Left:* UMAP representing 7 subsets from CD8⁺ T cells (n= 24,983). CM, central memory; MAIT, mucosal associated invariant T; TEMRA, terminally differentiated effector memory. *Right:* UMAPs of CD8⁺ T cells showing expression of select marker genes. **b,** UMAP color coded for CMV serostatus. **c,** *Left:* CD8⁺ T cell subset frequencies in CMV(-) and CMV(+). Cell types with significant frequency differences between CMV(-) and CMV(+) groups are marked with an asterisk (*; P-adjusted [Benjamini-Hochberg] < 0.05). *Right:* Select CD8⁺ T

cell frequencies within PBMCs quantified *via* scRNA-seq in Discovery Cohort: in CMV(-) (n=13) and CMV(+) (n=14). **d,** $CD8^+$ TEMRA cell frequencies within PBMCs quantified by flow cytometry in Validation Cohort: CMV(-) (n=23) and CMV(+) (n=40). **e,** Absolute count of $CD8^+$ TEMRA cells quantified by flow cytometry in Discovery Cohort: CMV(-) (n=8) and CMV(+) (n=8). **f,** γδ T cell frequencies within PBMCs quantified by flow cytometry in Validation Cohort: CMV(-) (n=23) and CMV(+) (n=40). **g,** $GZMK^+$ $CD8^+$, $GZMB^+$ γδ, and $CD8^+$ TEMRA T cell frequencies within PBMCs quantified *via* scRNA-seq in Cohort 3: CMV(+) (n=42) and CMV(-) (n=50). **h,** *Left:* UMAP representing 4 subsets from $CD4^+$ T cells (n= 55,927). Treg, $CD4^+$ T-regulatory; EM, effector memory; TEMRA, terminally differentiated effector memory. *Right:* UMAPs of $CD4^+$ T cells showing expression of select marker genes. **i,** UMAP color coded for CMV serostatus. **j,** *Left:* $CD4^+$ T cell subset frequencies in CMV(-) and CMV(+). Cell types with significant frequency differences between CMV(-) and CMV(+) groups are marked with an asterisk (*; P-adjusted [Benjamini-Hochberg] < 0.05). *Middle:* Naïve $CD4^+$ T cell frequencies within PBMCs. *Right:* $CD4^+$ TEMRA cell frequencies within PBMCs. All panels represent scRNA-seq data from Discovery Cohort: CMV(-) (n=13) and CMV(+) (n=14). **k,** $CD4^+$ TEMRA frequencies within PBMCs quantified by flow cytometry in Validation Cohort: CMV(-) (n=23) and CMV(+) (n=40). **l,** Absolute count of $CD4^+$ TEMRAs quantified by flow cytometry in Discovery Cohort: CMV(-) (n=8) and CMV(+) (n=8). **m,** $CD4^+$ TEMRA T cell frequencies within PBMCs quantified *via* scRNA-seq in Cohort 3: CMV(+) (n=42) and CMV(-) (n=50). Box plots display the median and IQR (25–75%), with whiskers representing the upper and lower quartiles ±1.5× IQR. Each dot represents an individual sample. Mann-Whitney-U test (two-sided) was used to compare cell counts between CMV(-) and CMV(+) (**c, d, e, f, g, j, k. l, m**). All *P*-values are shown after adjusting for multiple hypothesis testing using Benjamini-Hochberg at false discovery rate (FDR) < 0.05.

1022 **FIGURE 3**

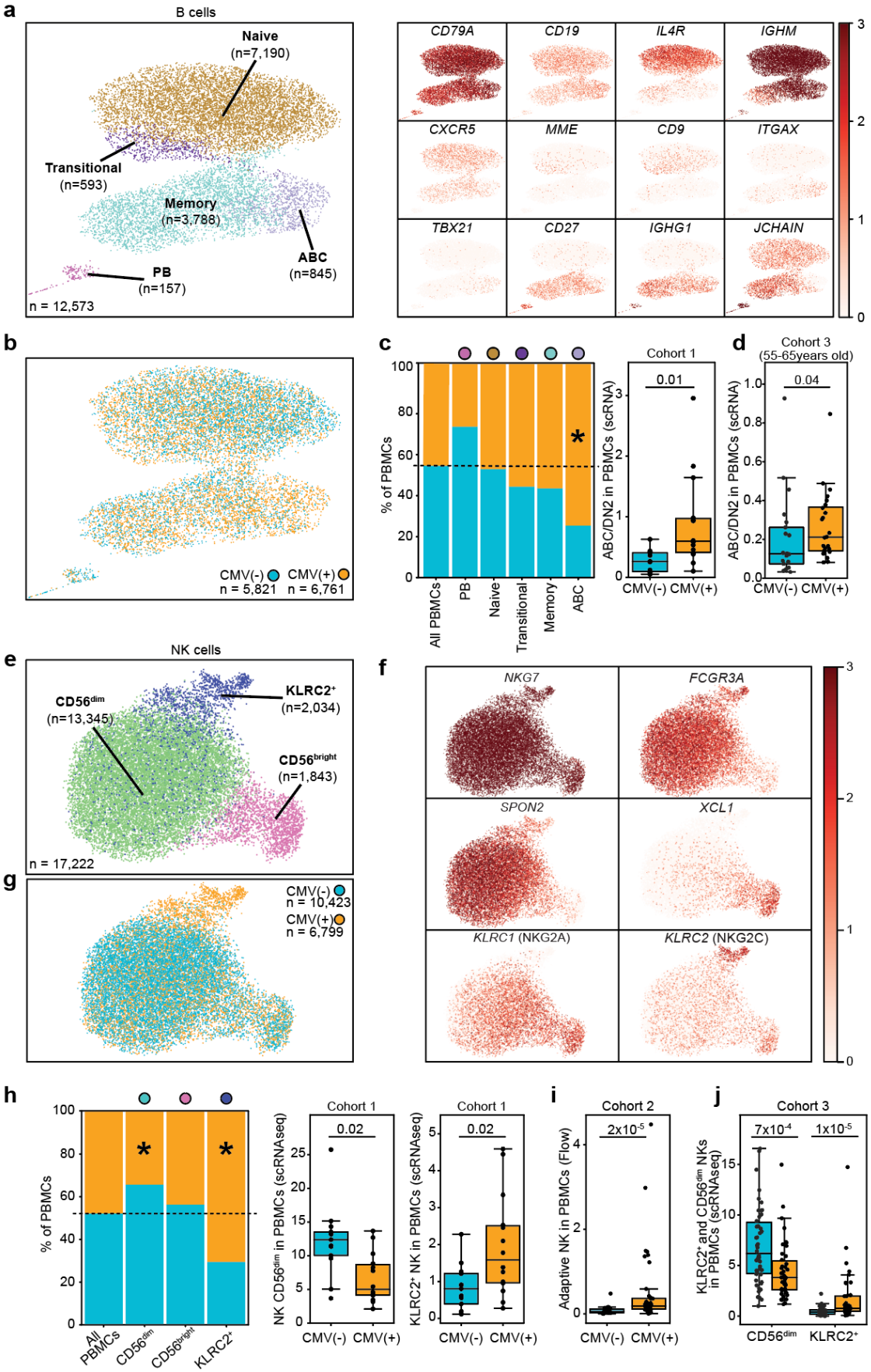
a
B cells
Naive
(n=7,190)
Transitional
(n=593)
Memory
(n=3,788)
ABC
(n=845)
PB
(n=157)
n = 12,573
CD79A
CD19
IL4R
IGHM
CXCR5
MME
CD9
ITGAX
TBX21
CD27
IGHG1
JCHAIN
b
CMV(-) n = 5,821
CMV(+) n = 6,761
c
% of PBMCs
All PBMCs
PB
Naive
Transitional
Memory
ABC
Cohort 1
0.01
ABC/DN2 in PBMCs (scRNA)
CMV(-) CMV(+)
d
Cohort 3
(55-65years old)
0.04
ABC/DN2 in PBMCs (scRNA)
CMV(-) CMV(+)
e
NK cells
CD56dim
(n=13,345)
KLRC2+
(n=2,034)
CD56bright
(n=1,843)
n = 17,222
f
NKG7
FCGR3A
SPON2
XCL1
KLRC1 (NKG2A)
KLRC2 (NKG2C)
g
CMV(-) n = 10,423
CMV(+) n = 6,799
h
% of PBMCs
All PBMCs
CD56dim
CD56bright
KLRC2+
Cohort 1
0.02
NK CD56dim in PBMCs (scRNAseq)
CMV(-) CMV(+)
Cohort 1
0.02
KLRC2+ NK in PBMCs (scRNAseq)
CMV(-) CMV(+)
i
Cohort 2
2x10-5
Adaptive NK in PBMCs (Flow)
CMV(-) CMV(+)
j
Cohort 3
7x10-4
1x10-5
KLRC2+ and CD56dim NKs in PBMCs (scRNAseq)
CD56dim
KLRC2+

1023

Fig. 3| ABC and adaptive NK cells were expanded while CD56^{dim}NK cells were reduced in CMV(+) older adults. a, *Left:* UMAP representing 5 B cell subsets (n= 12,573). PB, Plasmablast; ABC, atypical B cell. *Right:* UMAPs of B cells showing expression of select marker genes. **b,** UMAP color coded for CMV serostatus. **c,** *Left:* B cell frequencies in CMV(-) and CMV(+). Cell types with significant frequency differences between CMV(-) and CMV(+) groups are marked with an asterisk (*; P-adjusted [Benjamini-Hochberg] < 0.05). *Right:* ABC frequencies within PBMCs All panels represent scRNA-seq data from Discovery Cohort: CMV(-) (n=13) and CMV(+) (n=14). **d,** ABC frequencies within PBMCs quantified *via* scRNA-seq in Cohort 3 (55-65 age group): CMV(+) (n=24) and CMV(-) (n=20). **e,** UMAP representing 3 NK cell subsets (n= 17,222). **f,** UMAPs of NK cells showing expression of select marker genes. **g,** UMAP color coded for CMV serostatus. **h,** *Left:* NK cell frequencies in CMV(-) and CMV(+). Cell types with significant frequency differences between CMV(-) and CMV(+) groups are marked with an asterisk (*; P-adjusted [Benjamini-Hochberg] < 0.05). *Middle:* NK CD56^{dim} frequencies within PBMCs. *Right:* KLRC2^{+} NK cell frequencies within PBMCs. All panels represent scRNA-seq data from Discovery Cohort: CMV(-) (n=13) and CMV(+) (n=14). **i,** Adaptive NK frequencies within PBMCs quantified by flow cytometry in Validation Cohort: CMV(-) (n=23) and CMV(+) (n=40). **j,** NK CD56^{dim} and KLRC2^{+} NK cell frequencies quantified *via* scRNA-seq in Cohort 3: CMV(+) (n=42) and CMV(-) (n=50). Box plots display the median and IQR (25–75%), with whiskers representing the upper and lower quartiles ±1.5× IQR. Each dot represents an individual sample. For Mann-Whitney-U test (two-sided) was used to compare cell counts between CMV(-) and CMV(+) (**c**, **d, h, i, j**). All *P*-values are shown after adjusting for multiple hypothesis testing using Benjamini-Hochberg at false discovery rate (FDR) < 0.05.

1048 **FIGURE 4**

1049

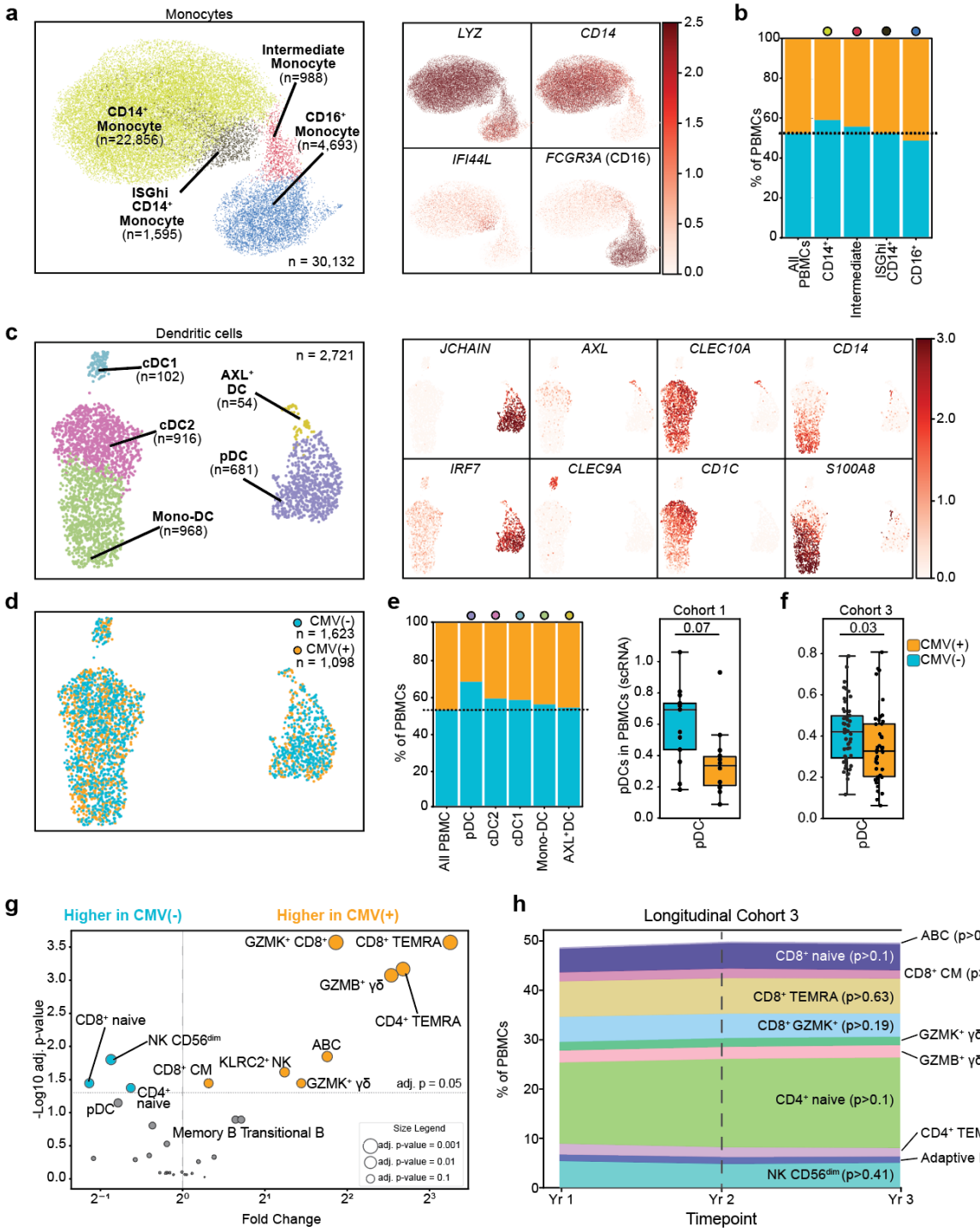

1050

1051 **Fig. 4| Monocytes and dendritic cells were comparable between CMV(+) and CMV(-) older**
1052 **adults. a,** *Left:* UMAP representing 4 monocyte subsets (n= 30,132). ISGhi, interferon stimulated
1053 gene-high expressing subset. *Right:* UMAPs of monocytes showing expression of select marker
1054 genes. **b,** Monocyte frequencies in CMV(-) and CMV(+). **c,** *Left:* UMAP representing 5 DC
1055 subsets (n= 2,721). DC, dendritic cell; Mono-DC, monocyte-derived dendritic cell; cDC1,
1056 conventional type 1 dendritic cells; cDC2, Conventional type 2 dendritic cells; pDC, plasmacytoid

dendritic cell. *Right:* UMAPs of DCs showing expression of select marker genes. **d,** UMAP color coded for CMV serostatus. **e,** *Left:* DC frequencies in CMV(-) and CMV(+). *Right:* pDC frequencies within PBMCs. All panels represent scRNA-seq data from Discovery Cohort: CMV(-) (n=13) and CMV(+) (n=14). **f,** pDC frequencies quantified *via* scRNA-seq in Cohort 3: CMV(+) (n=42) and CMV(-) (n=50). **g,** Summary volcano plot showing PBMC compositional alterations associated with CMV serostatus in Discovery Cohort. Size of bubbles represent p-adjusted value (-Log scale). **h,** Average frequencies of CMV-associated cell types over a three-year period in CMV(+) individuals from Cohort 3 (n=22). For **e,** and **f,** box plots display the median and IQR (25–75%), with whiskers representing the upper and lower quartiles ±1.5× IQR. Each dot represents an individual sample. Mann-Whitney-U test (two-sided) was used to compare cell counts (**e, f, h**). All *P*-values are shown after adjusting for multiple hypothesis testing using Benjamini-Hochberg at false discovery rate (FDR) < 0.05.

1071 **FIGURE 5**

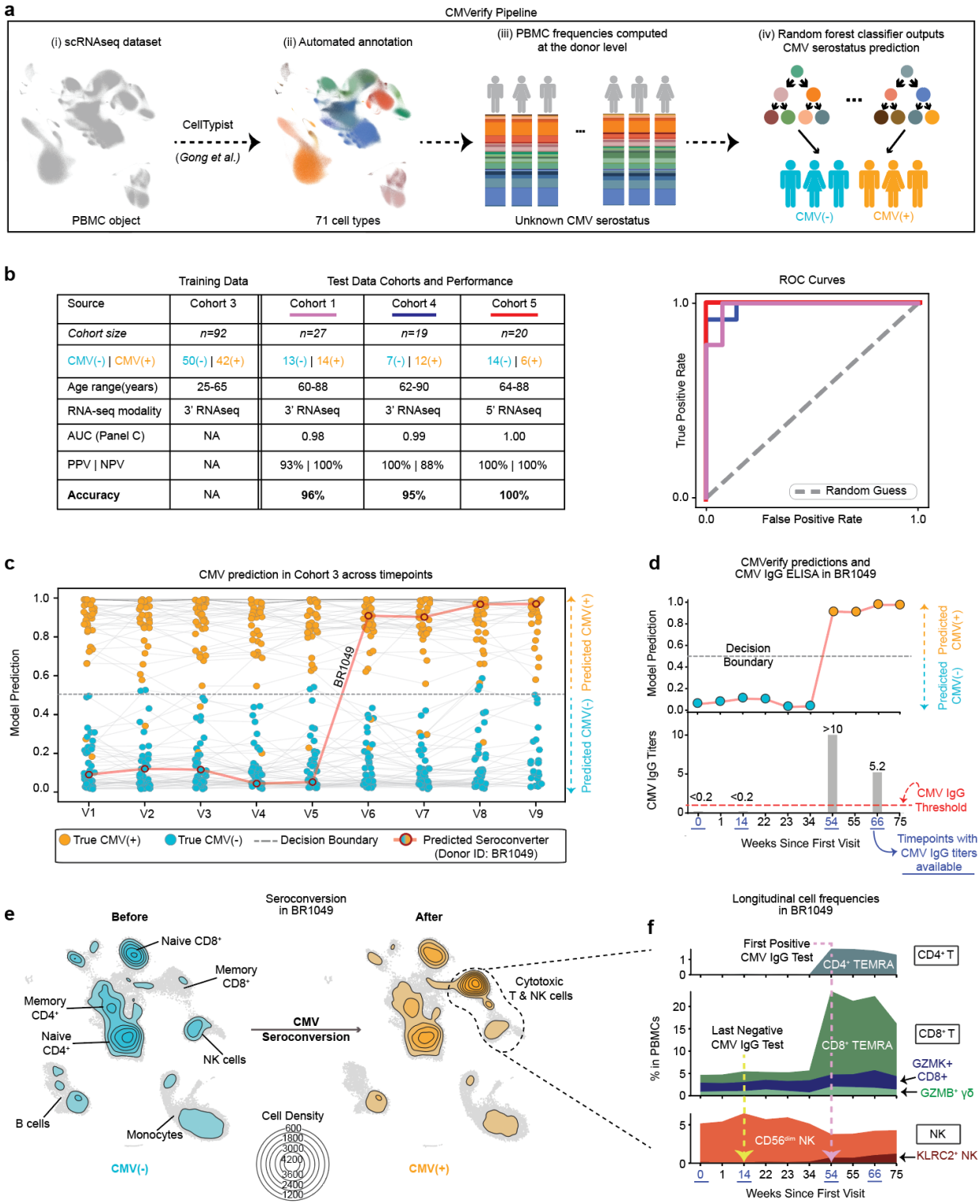

Source	Training Data: Cohort 3	Test Data Cohorts and Performance: Cohort 1	Cohort 4	Cohort 5
Cohort size	*n=92*	*n=27*	*n=19*	*n=20*
CMV(-) | CMV(+)	50(-) | 42(+)	13(-) | 14(+)	7(-) | 12(+)	14(-) | 6(+)
Age range(years)	25-65	60-88	62-90	64-88
RNA-seq modality	3' RNAseq	3' RNAseq	3' RNAseq	5' RNAseq
AUC (Panel C)	NA	0.98	0.99	1.00
PPV | NPV	NA	93% | 100%	100% | 88%	100% | 100%
Accuracy	NA	**96%**	**95%**	**100%**

1072
1073
1074 **Fig. 5| *CMVerify*—a novel tool that accurately predicts CMV serostatus from scRNA-seq**
1075 **data. a,** Schematic representation of *CMVerify* Pipeline: (i) *CMVerify* accepts a PBMC scRNA-
1076 seq dataset as input, (ii) applies CellTypist to automatically annotate the dataset, (iii) computes
1077 PBMC frequencies at the donor level, and (iv) uses a random forest classifier to predict CMV

serostatus. **b,** *Left*: Table summarizing *CMVerify's* training dataset and performance in three independent test cohorts spanning different age groups and scRNA-seq modalities. PPV, positive predictive value; NPV, negative predictive value; *Right*: Receiver Operating Characteristic (ROC) curves showing performance of *CMVerify* in the independent cohorts. **c,** *CMVerify* prediction results for the Cohort 3 longitudinal data. Y-axis represents model predicted probability, each bubble is a unique sample corresponding with a donor timepoint. Samples from the same donor are connected via gray lines. Based on the Decision Boundary ($y = 0.5$), all bubbles below the Decision Boundary ($y < 0.5$) represent prediction of CMV(-), vs. bubbles above the Decision boundary ($y > 0.5$) represent prediction of CMV(+). Bubbles are color coded for true CMV serostatus (determined via CMV IgG ELISA). Red line connects model predicted probabilities for the seroconverter (donor ID: BR1049; $n = 1$) across all timepoints ($n = 9$). **d,** *Top*: *CMVerify* prediction probabilities across all timepoints in donor BR1049 identified in panel **c**. *Bottom*: CMV IgG titers for donor BR1049. Underlined timepoints (in blue) indicate presence of CMV IgG data at those timepoints. The red dotted line indicates CMV IgG titer threshold above which a sample is considered CMV(+). **e**, Contour UMAP plots show PBMC densities before and after CMV seroconversion in donor BR1049. The UMAP labeled 'Before' includes timepoints at weeks 14, 22, 23, and 34, while the UMAP labeled 'After' includes weeks 54, 55, 66, and 75. The Cell Density legend indicates the number of cells within each contour level shown in the UMAPs. **f**, CMV-driven changes in Cytotoxic T and NK cell frequencies over time in donor BR1049.

FIGURE 6

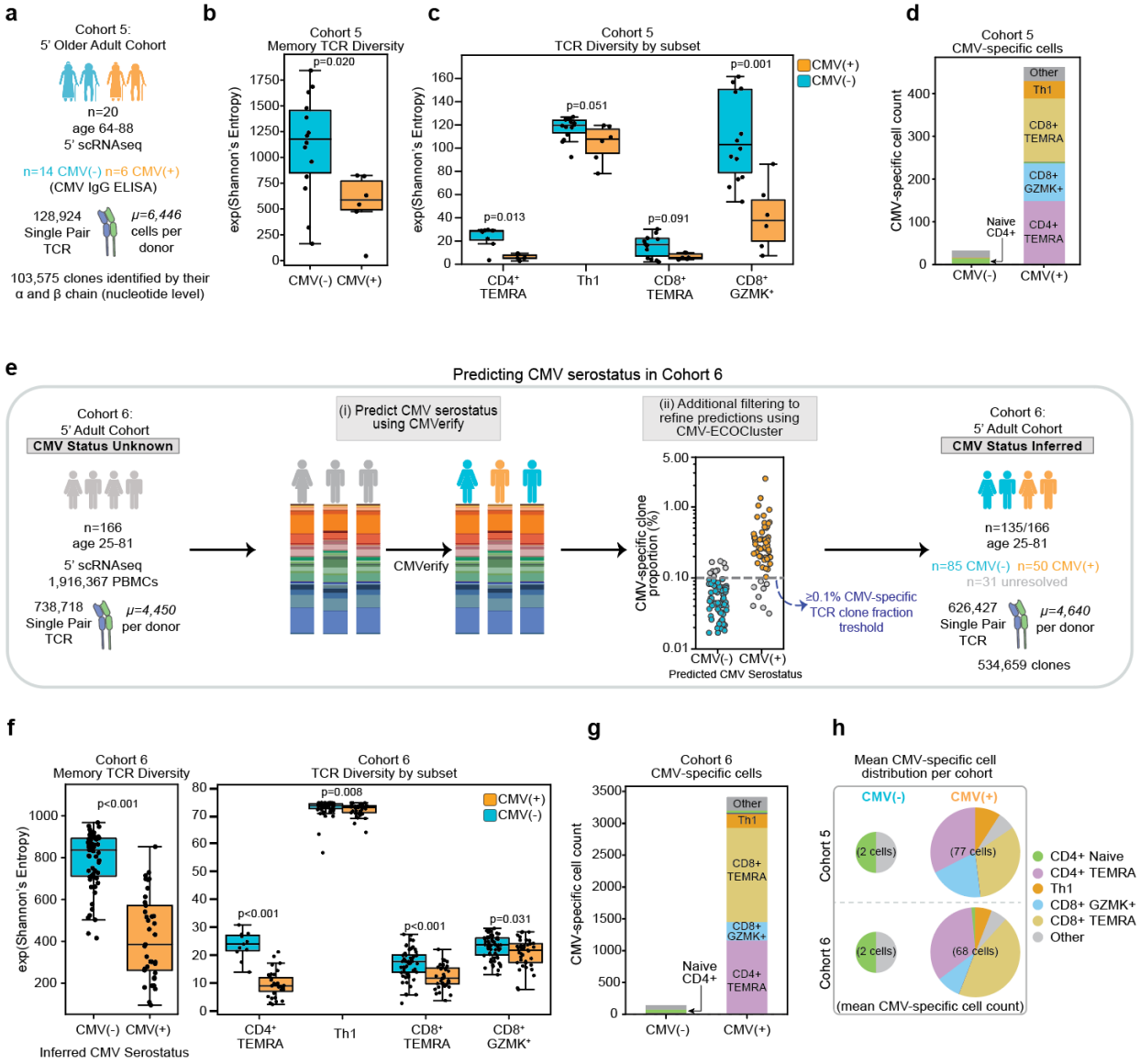

Fig. 6| Putative CMV-specific TCR clones are expanded in GZMK$^+$ CD8$^+$ and Th1 T cells. **a**, Cohort 2 included *n=14* CMV(-) and *n=6* CMV(+) older adults profiled using 5' scRNAseq with paired scTCR-seq. **b**, Cohort 2 TCR diversity in memory T cells. **c,** Cohort 2 TCR diversity in CD4$^+$/CD8$^+$ TEMRA, Th1, and CD8$^+$ GZMK$^+$ T subsets. **d**, Cohort 2 putative CMV-specific cell counts identified by exact matching with the CMV ECOcluster (see Methods). **e**, Schematic representation of method to infer CMV serostatus in Cohort 3 (*n=166* donors with CMV status unknown). (i) predict CMV serostatus using CMVerify, (ii) additional filtering to refine CMVerify predictions based on the fraction of putative CMV-specific clones: <0.1% in predicted CMV(–) individuals and ≥0.1% in predicted CMV(+) individuals. The gray line (y = 0.1%) indicates the cutoff threshold (derived from Cohort 2 with ELISA CMV IgG; Extended Data Fig. 7d). In total, CMV-serostatus was confidently inferred for 135/166 individuals in Cohort 3. **f**, *Left:* Cohort 3 TCR diversity in memory T cells. *Right:* Cohort 3 TCR diversity in CD4$^+$/CD8$^+$ TEMRA, Th1, and CD8$^+$ GZMK$^+$ T subsets. **g**, Cohort 3 putative CMV-specific cell counts identified by exact matching with the CMV ECOcluster. **h**, Distribution of CMV-specific TCR by cell type in CMV(-) and CMV(+) individuals, grouped by cohort.. The size of each pie chart

represents the average number of CMV-specific cells (log scale). The mean CMV-specific cell count per group and cohort is indicated in parentheses. For **b, c,** and **f,** box plots display the median and IQR (25–75%), with whiskers representing the upper and lower quartiles ±1.5× IQR. Each dot represents an individual sample. Mann-Whitney-U test (two-sided) was used to compare differences between groups. TCR diversity was calculated using Shannon's entropy (e^H). For **c**, due to the small sample size in the CMV(+) group (6/20), diversity calculations within cell types were not FDR-corrected. For **f**, *P*-values shown are after adjusting for multiple hypothesis testing using Benjamini-Hochberg at false discovery rate (FDR) < 0.05.

Extended Figure 1:

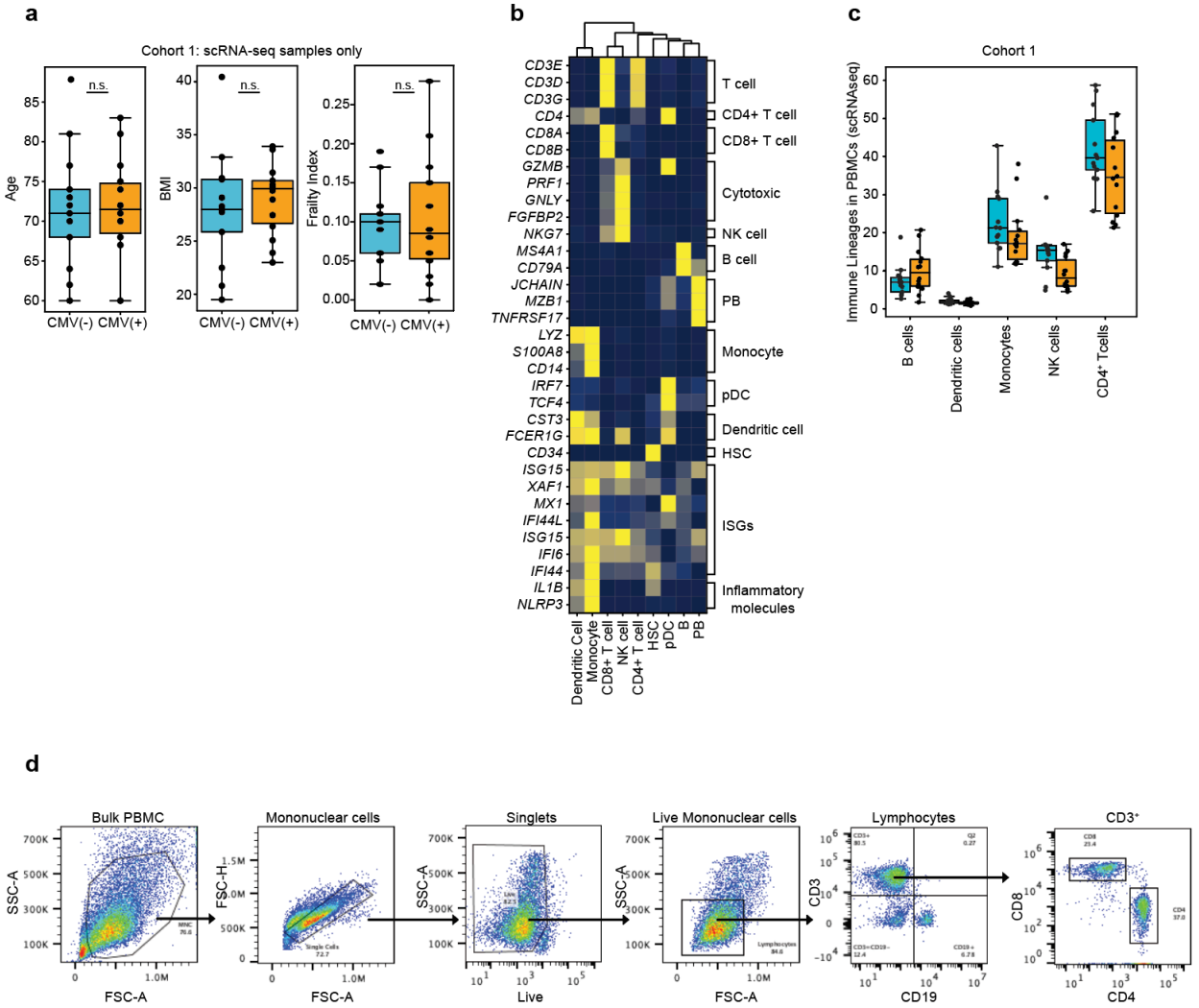

Extended Data Fig. 1: PBMC-level annotations and analysis. a, Distribution of age, BMI, and frailty index in Discovery Cohort (scRNA-seq samples only n=27). n.s. indicates not significant. **b,** Scaled expression of select marker genes. **c,** PBMC subset frequency ratios quantified *via* scRNA-seq in CMV(-) (n=13) and CMV(+) (n=14) in Discovery Cohort. **d**, Gating strategy for $CD8^+$ and $CD4^+$ T cells in Cohort 2 using flow cytometry; FSC, forward scatter; SSC, side scatter. Box plots display the median and IQR (25–75%), with whiskers representing the upper and lower quartiles ±1.5× IQR. Each dot represents an individual sample. For a and c, Mann-Whitney-U test (two-sided) was used to calculate *P*-values between CMV(-) and CMV(+). **c**, none of the measurements were significant after adjusting the *P*-values for multiple hypothesis testing, using Benjamini-Hochberg at false discovery rate (FDR) < 0.05.

Extended Figure 2:

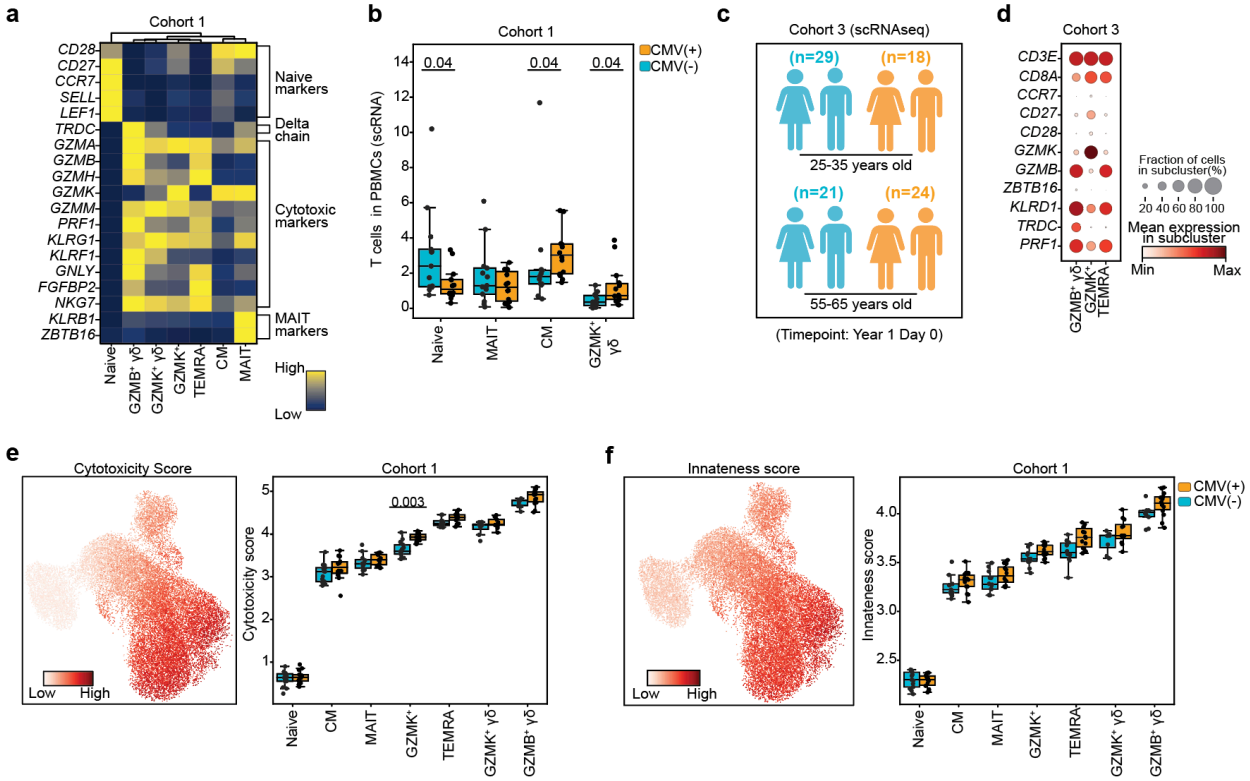

Extended Data Fig. 2: Cytotoxicity and innateness scores for CD8$^+$ T cell subsets. a, Scaled expression of select marker genes in CD8$^+$ T cell subsets. **b,** Select CD8$^+$ T cell frequencies within PBMCs quantified *via* scRNA-seq in Discovery Cohort: CMV(-) (n=13) and CMV(+) (n=14). **c,** Gating strategy for CD8$^+$/CD4$^+$ TEMRA and γδ T cells in Cohort 2 using flow cytometry; FSC, forward scatter; SSC, side scatter. **d,** Schematic representation of Cohort 3 including two age groups (25-35 years old; 55-65 years old). **e,** Scaled expression of select marker for GZMB$^+$ γδ T, GZMK$^+$ T, and CD8$^+$ TEMRA T cells in Cohort 3. **f,** *Left:* UMAP showing Cytotoxicity score in CD8$^+$ T cell subsets. *Right:* individual-level cytotoxicity score in CD8$^+$ T cells subsets. **g,** *Left:* UMAP showing Innateness score in CD8$^+$ T cell subsets. *Right:* individual-level Innateness score in CD8$^+$ T cells subsets. Box plots display the median and IQR (25–75%), with whiskers representing the upper and lower quartiles ±1.5× IQR. Each dot represents an individual sample. Mann-Whitney-U test (two-sided) was used to compare cell counts between CMV(-) and CMV(+) (**b, f, g**). All *P*-values are shown after adjusting for multiple hypothesis testing using Benjamini-Hochberg at false discovery rate (FDR) < 0.05.

Extended Figure 3:

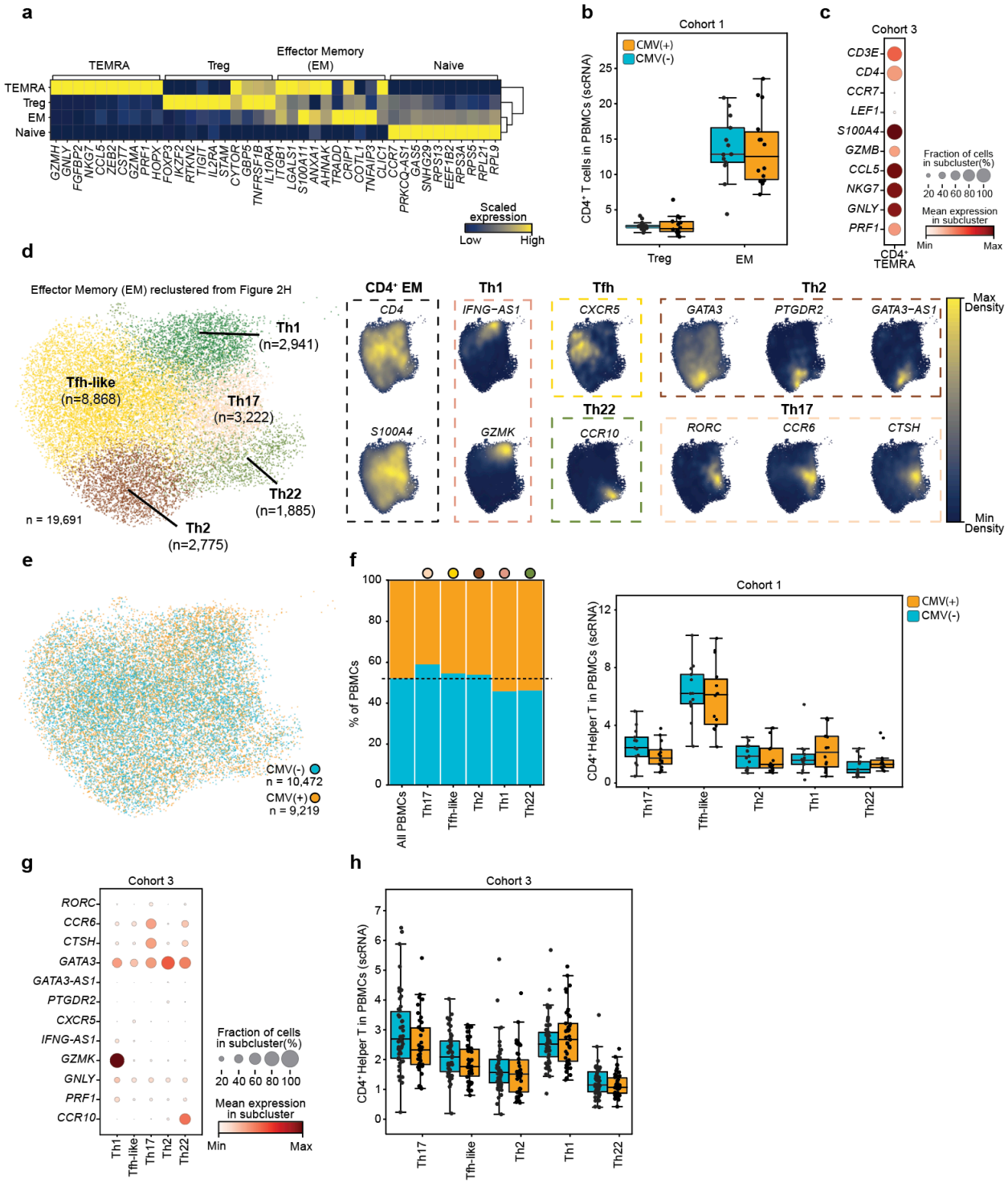

Extended Data Fig. 3: CD4$^+$ T helper subsets were comparable between CMV(-) and CMV(+). a, Scaled expression of top 10 marker genes in CD4$^+$ naïve, CD4$^+$ Treg, CD4$^+$ EM, and CD4$^+$ TEMRA subsets. **b,** CD4$^+$ Treg and CD4$^+$ TEMRA T cell frequencies within PBMCs quantified *via* scRNA-seq in Discovery Cohort: CMV(-) (n = 13) and CMV(+) (n = 14). **c,** Scaled expression of select marker genes for CD4$^+$ TEMRA T cells in Cohort 3. **d,** *Left:* UMAP

representing re-clustered $CD4^+$ EM compartment and 5 resulting T helper subsets. Tfh-like, T follicular helper-like; Th2, T helper 2; Th22, T helper 22; Th17, T helper 17; Th1. *Right:* Gene density plot showing expression levels of key marker genes, calculated using Nebulosa. Each gene density is grouped according to known T helper marker genes. **e,** UMAP color coded for CMV serostatus. **f,** *Left:* $CD4^+$ T helper frequencies in CMV(-) and CMV(+). *Right:* T helper cell frequencies within PBMCs quantified *via* scRNA-seq in Discovery Cohort: CMV(-) (n=13) and CMV(+) (n=14). **g,** Scaled expression of select marker genes for T helper subsets in Cohort 3. **h,** T helper cell frequencies within PBMCs quantified *via* scRNA-seq in Cohort 3: CMV(+) (n=42) and CMV(-) (n=50). Box plots display the median and IQR (25–75%), with whiskers representing the upper and lower quartiles ±1.5× IQR. Each dot represents an individual sample. Mann-Whitney-U test (two-sided) was used to compare cell counts between CMV(-) and CMV(+) (**b**, **e,** **h,**). None of the measurements were significant after adjusting the *P*-values for multiple hypothesis testing, using Benjamini-Hochberg at false discovery rate (FDR) < 0.05.

Extended Figure 4:

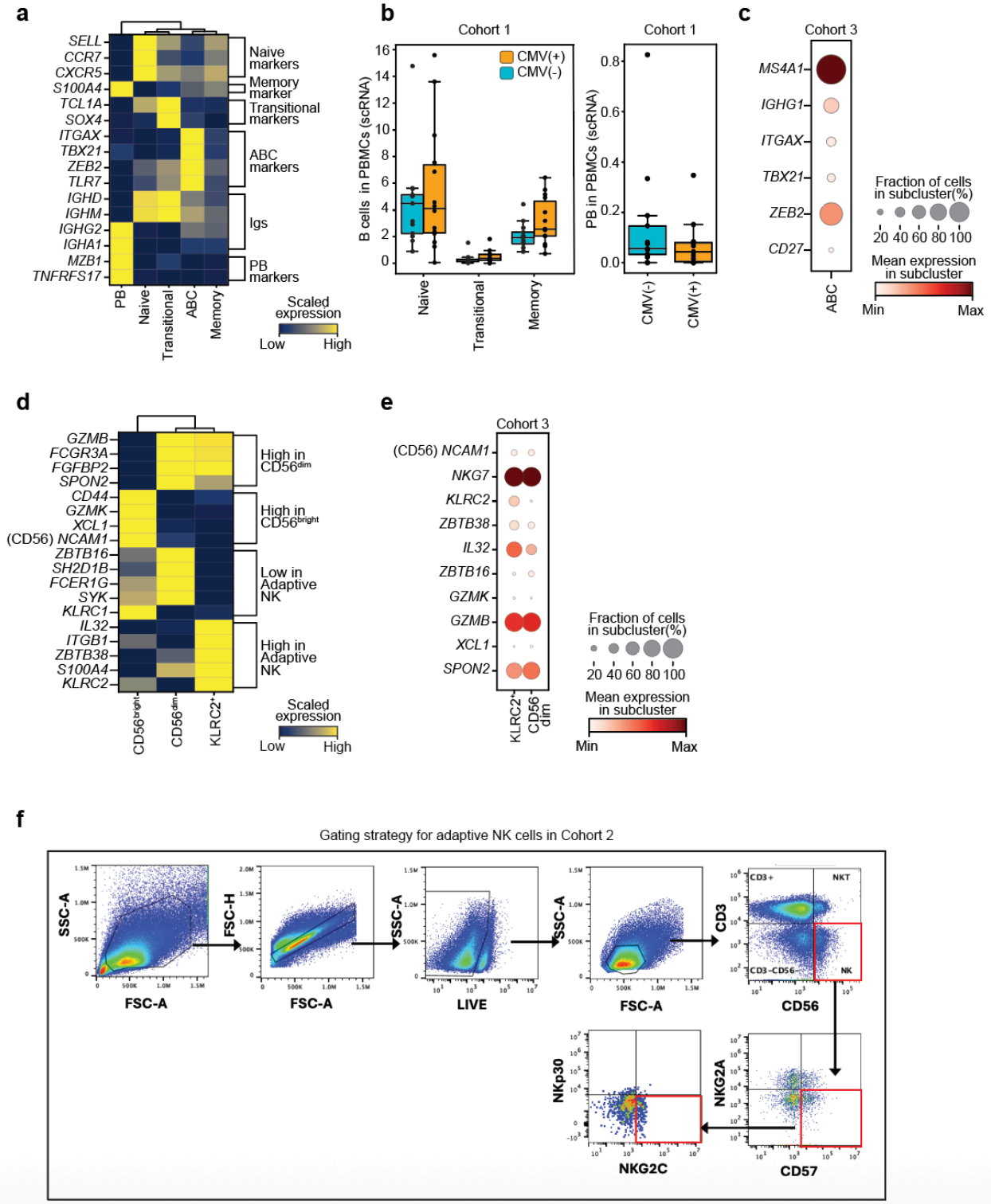

Extended Data Fig. 4: B and NK cell annotations. a, Scaled expression of select marker genes in B cell subsets. **b,** *Left:* naïve, transitional, and memory B cell frequencies within PBMCs. *Right:* PB cell frequencies within PBMCs. All panels represent scRNA-seq data from Discovery Cohort: CMV(-) (n=13) and CMV(+) (n=14). **c,** Scaled expression of select marker genes for ABCs in

Cohort 3. **d,** Scaled expression of select marker genes in NK cell subsets. **e,** Scaled expression of select marker genes for KLRC2^{+} and CD56^{dim} NK cells in Cohort 3. **f,** Gating strategy for adaptive NK cells in Cohort 2 using flow cytometry; FSC, forward scatter; SSC, side scatter. Box plots display the median and IQR (25–75%), with whiskers representing the upper and lower quartiles ±1.5× IQR. Each dot represents an individual sample. Mann-Whitney-U test (two-sided) was used to compare cell counts between CMV(-) and CMV(+) (**b**). None of the measurements were significant after adjusting the *P*-values for multiple hypothesis testing, using Benjamini-Hochberg at false discovery rate (FDR) < 0.05.

Extended Figure 5:

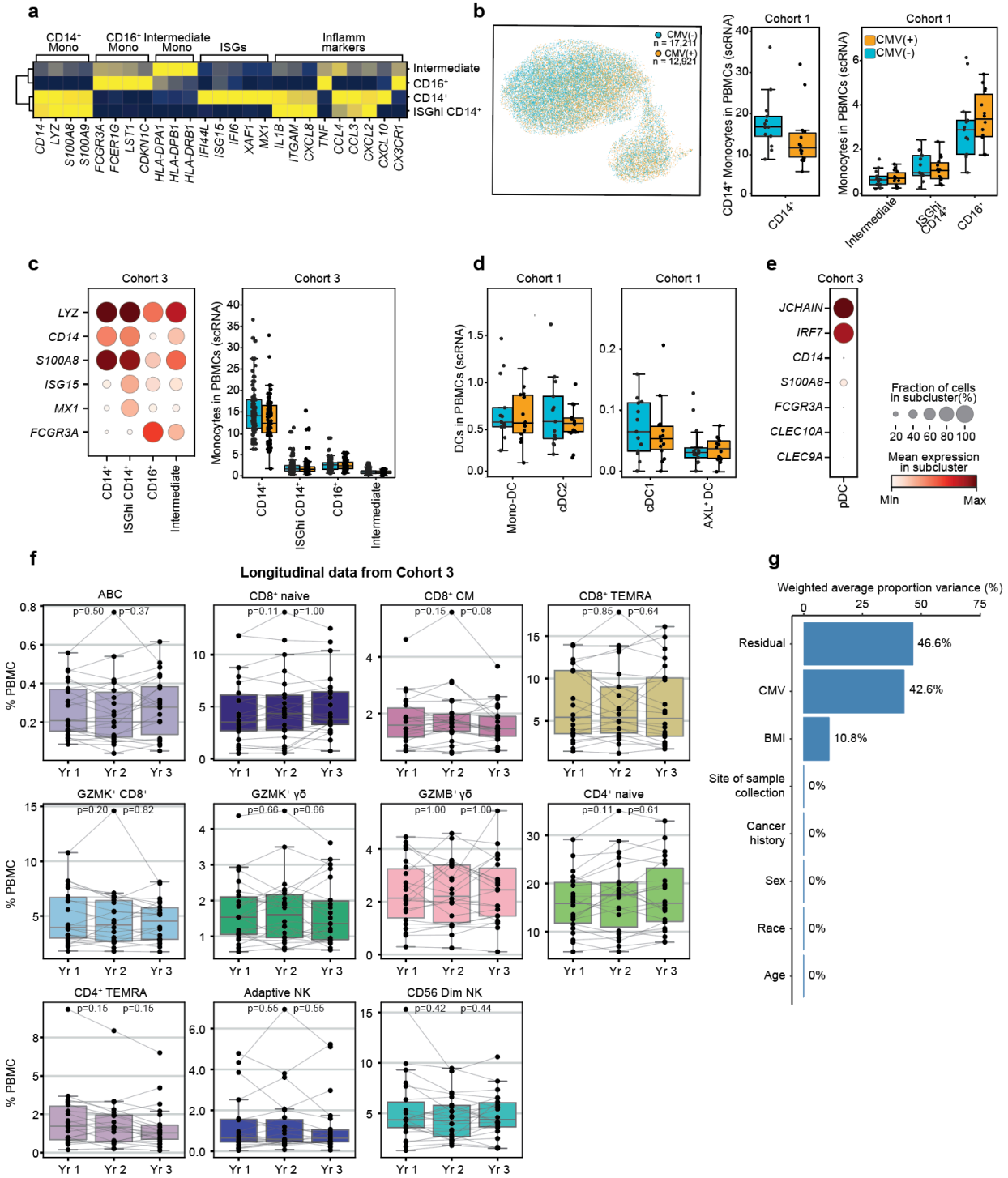

Extended Data Fig. 5: Monocyte subset annotations and temporal stability of PBMC frequencies associated with CMV. a, Scaled expression of select marker genes in monocyte subsets. **b,** *Left:* UMAP color coded for CMV serostatus. *Middle:* CD14^{+} monocyte frequencies within PBMCs. *Right:* Intermediate, ISGhi CD14^{+}, and CD16^{+} monocyte frequencies within PBMCs. All panels represent scRNA-seq data from Discovery Cohort: CMV(-) (n=13) and

CMV(+) (n=14) **c,** *Left:* scaled expression of select marker genes for $CD14^+$, ISGhi $CD14^+$, and $CD16^+$, and intermediate monocytes. *Right:* monocyte subset frequencies within PBMCs. All panels represent scRNA-seq data from Cohort 3: CMV(+) (n=42) and CMV(-) (n=50). **d,** *Left:* Mono-DC, and cDC2 frequencies within PBMCs. *Right:* cDC1 and AXL^+ DC frequencies within PBMCs. All panels represent scRNA-seq data from Discovery Cohort: CMV(-) (n=13) and CMV(+) (n=14). **e,** Scaled expression of select marker genes for pDCs in Cohort 3. **f,** Individual-level frequencies of CMV-associated cell types over a three-year period in CMV(+) individuals from Cohort 3 (n=22). Connecting lines represent individual-specific changes in cell frequencies between Year 1, Year 2, and Year 3 visits. *P*-values in each box plot are shown for **i,** Year 1-Year 2 and (ii) Year 2-Year 3 comparisons. **g**, Principal Variance Component Analysis (PVCA) of lymphocyte subset frequencies, estimating the proportion of variance explained by each clinical factor in Cohort 1 . Box plots display the median and IQR (25–75%), with whiskers representing the upper and lower quartiles ±1.5× IQR. Each dot represents an individual sample. Mann-Whitney-U test (two-sided) was used to compare cell counts (**b**, **d, f**). None of the measurements were significant after adjusting the *P*-values for multiple hypothesis testing, using Benjamini-Hochberg at false discovery rate (FDR) < 0.05.

Extended Figure 6:

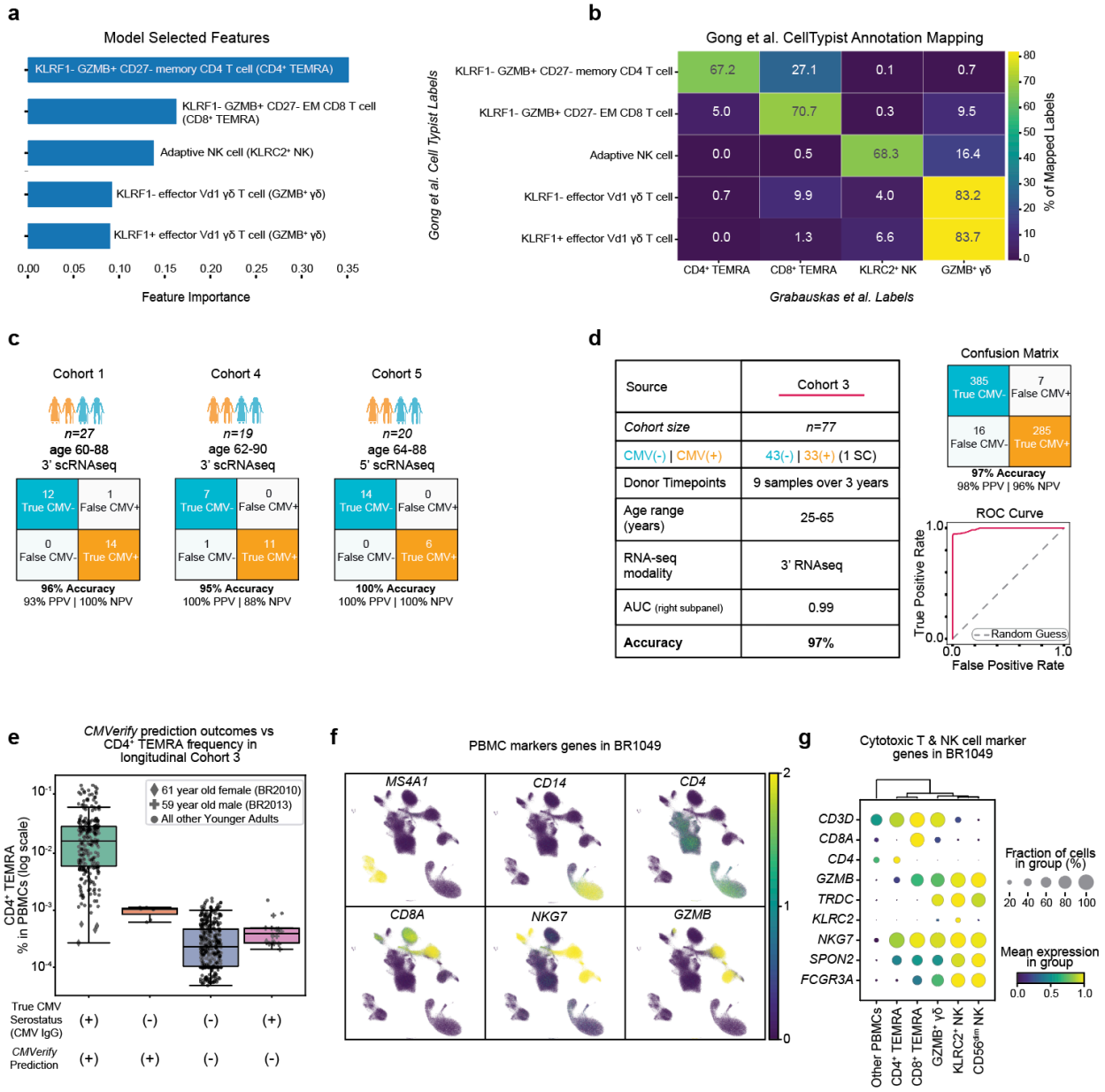

Extended Data Fig. 6: *CMVerify* selected features and extended prediction metrics. a, Top 5 selected features by *CMVerify* during the training procedure (see Methods) to predict CMV serostatus. Cell type labels were determined via the AIFI_L3 CellTypist model.[32] **b,** Heatmap showing percent of cell type labels mapped from AIFI_L3 CellTypist model to manual labels in our study. **c,** Confusion matrices for CMV serostatus prediction in each independent cohort from **Fig. 5b**. **d,** *Left*: table summarizing the longitudinal Cohort 3. '1 SC' stands for 'one seroconverter' (donor ID: BR1049). *Right top*: Confusion matrix for CMV serostatus predictions from the longitudinal Cohort 3 in **Fig. 5d**. *Right lower*: Receiver Operating Characteristic (ROC) curve quantifying performance of *CMVerify* on the longitudinal Cohort 3 in **Fig. 5d**. **e,** CMVerify prediction outcomes and CD4+ TEMRA frequencies per sample in the longitudinal Cohort 3.

1240 Diamonds represent the 61-year-old female (donor ID: BR2010), misclassified at five timepoints.
1241 Crosses represent the 59-year-old male (donor ID: BR2013), misclassified at nine timepoints.
1242 Circles represent all other samples. **f**, Expression of PBMC marker genes in donor BR1049 across
1243 all timepoints shown in **Fig. 5e. g,** Expression of cytotoxic marker genes in select PBMC subsets
1244 from **Fig. 5f**. PPV, positive predictive value; NPV, negative predictive value (**c,d**).
1245
1246
1247

Extended Figure 7:

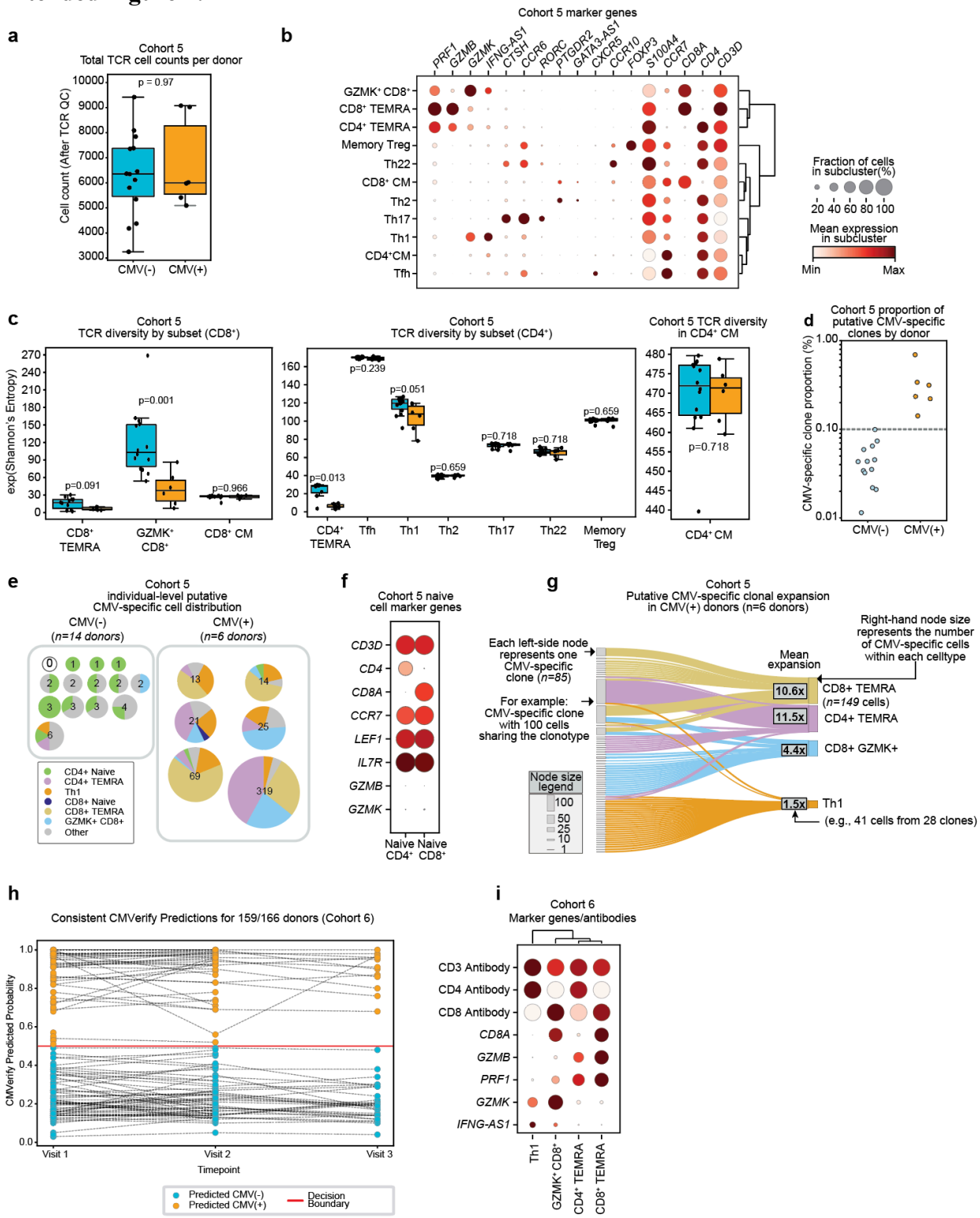

Extended Data Fig. 7: TCR diversity and CMV-specific clonal expansions in Cohorts 2 and 3. a, Total TCR cell counts after quality control in Cohort 2. **b,** Expression of marker genes in TCR-profiled cells in Cohort 2. **c,** TCR diversity in CD8$^+$ and CD4$^+$ T cells in Cohort 2. **d,** Putative CMV-specific clone proportion per donor in Cohort 2. **e,** Pie charts showing putative CMV-specific cell types per donor in CMV(–) and CMV(+) groups. Each pie chart corresponds to a

donor in Cohort 2, where the sizerepresents the number of CMV-specific cells detected (log scale). One CMV(-) donor had no putative CMV-specific cell types, indicated by '0.'**f**, Expression of naïve marker genes in TCR-profiled cells in Cohort 2. **g,** Sankey plot of putative CMV-specific clones and their corresponding cells in CMV(+) individuals from Cohort 2. Each node on the left represents one putative CMV-specific clone, with thenode size proportional to the number of cells sharing the clonotype. Nodes on the right represent annotated cell types, with node size proportional to the number of putative CMV-specific cells detected within the celltype. **h,** Longitudinal CMVerify predictions for each individual in Cohort 3. Y-axis represents model predicted probability, each bubble is a unique sample corresponding with a donor timepoint. Samples from the same donor are connected via gray lines. Based on the Decision Boundary ($y = 0.5$), all bubbles below the Decision Boundary ($y < 0.5$) represent prediction of CMV(-), vs. bubbles above the Decision boundary ($y > 0.5$) represent prediction of CMV(+). Bubbles are color coded for CMVerify prediction based on the prediction probability. **i**, Expression of marker genes and antibody staining in select TCR-profiled cells in Cohort 3. For **a** and **c,** box plots display the median and IQR (25–75%), with whiskers representing the upper and lower quartiles ±1.5× IQR. Each dot represents an individual sample. Mann-Whitney-U test (two-sided) was used to compare differences between groups. For **c**, TCR diversity was calculated using Shannon's entropy (e^H). Additionally, due to the small sample size in the CMV(+) group (6/20), diversity calculations within cell types were not FDR-corrected.